CellPress

Chemistry & Biology
Resource

Photoswitchable Red Fluorescent Protein with a Large Stokes Shift

Kiryl D. Piatkevich,[1] Brian P. English,[1,4] Vladimir N. Malashkevich,[2] Hui Xiao,[3] Steven C. Almo,[2] Robert H. Singer,[1,4] and Vladislav V. Verkhusha[1,5,*]
[1]Department of Anatomy and Structural Biology
[2]Department of Biochemistry
[3]Department of Pathology
Albert Einstein College of Medicine, Bronx, NY 10461, USA
[4]Janelia Farm Research Campus, Howard Hughes Medical Institute, Ashburn, VA 20147, USA
[5]Department of Biochemistry and Developmental Biology, Institute of Biomedicine, University of Helsinki, Helsinki 00290, Finland
*Correspondence: vladislav.verkhusha@einstein.yu.edu
http://dx.doi.org/10.1016/j.chembiol.2014.08.010

SUMMARY

A subclass of fluorescent proteins (FPs), large Stokes shift (LSS) FP, are characterized by increased spread between excitation and emission maxima. We report a photoswitchable variant of a red FP with an LSS, PSLSSmKate, which initially exhibits excitation and emission at 445 and 622 nm, but violet irradiation photoswitches PSLSSmKate into a common red form with excitation and emission at 573 and 621 nm. We characterize spectral, photophysical, and biochemical properties of PSLSSmKate in vitro and in mammalian cells and determine its crystal structure in the LSS form. Mass spectrometry, mutagenesis, and spectroscopy of PSLSSmKate allow us to propose molecular mechanisms for the LSS, pH dependence, and light-induced chromophore transformation. We demonstrate the applicability of PSLSSmKate to superresolution photoactivated localization microscopy and protein dynamics in live cells. Given its promising properties, we expect that PSLSSmKate-like phenotype will be further used for photoactivatable imaging and tracking multiple populations of intracellular objects.

INTRODUCTION

Fluorescent proteins (FPs) of the GFP-like protein family are among the most widely used optical probes, with a wide range of applications in modern biology as noninvasive tools for spatial and temporal visualization of cellular structures, intermolecular interactions, gene expression, and tracking intracellular movements (Chudakov et al., 2010; Miyawaki et al., 2012; Shcherbakova et al., 2012b; Wu et al., 2011). The central component of all FPs is a chromophore, typically consisting of a conjugated π-electron system. Despite the highly conserved 3D structure, consisting of a β-barrel formed by 220 to 240 amino acids, GFP-like FPs exhibit a vast variety of chromophore chemical structures (Chudakov et al., 2010; Miyawaki et al., 2012; Subach and Verkhusha, 2012). The precise chemical and structural features of a chromophore, and its interactions with the immediate protein environment, are responsible for the FP spectral properties. In addition to fluorescence, photon absorption by a chromophore can induce photochemical or photophysical transformations in FPs. These transformations can lead to chemical modification of the chromophore or its environment, giving rise to modified FPs with altered spectral features.

The ability to modulate spectral properties of FPs with light is particularly useful for superresolution microscopy and studies of protein dynamics in cells. Numerous photocontrollable FPs of different hues were developed by means of rational design and directed molecular evolution (Chudakov et al., 2010; Piatkevich and Verkhusha, 2010; Subach et al., 2011a). Currently available photocontrollable FPs can be categorized on the basis of their spectral properties into three major groups: photoactivatable FPs (PAFPs), photoswitchable FPs (PSFPs) and reversibly photoswitchable FPs (rsFPs). While PAFPs undergo activation from a dark (nonfluorescent) state to a fluorescent state, PSFPs can be converted from one fluorescent state to another. In contrast to PAFPs and PSFPs, which could be photoactivated only once (irreversibly), rsFPs can be repeatedly photoswitched between dark and fluorescent states.

Photoswitching in GFP-like FPs was described shortly after the cloning of wild-type GFP (wtGFP) from *A. victoria* (Chalfie et al., 1994; Cubitt et al., 1995). It was noticed that UV and violet light reduced the Stokes shift of wtGFP, converting the species with neutral chromophore that absorbs at 398 nm into an anionic species absorbing at 478 nm (Chattoraj et al., 1996). Subsequent structural and spectroscopic studies allowed understanding the molecular mechanisms for the photoinduced modulation of Stokes shift in wtGFP. The crystal structure of wtGFP revealed that the hydroxyphenyl group of the chromophore forms a hydrogen bond with the carboxyl group of Glu222 via water molecule and Ser205 (Palm et al., 1997). This hydrogen bond interaction keeps a GFP-like chromophore protonated in the ground state. However, upon illumination with violet light, the excited state of the neutral chromophore rapidly converts to an excited anionic state via proton transfer from the hydroxyphenyl group of the chromophore to Glu222. After emission of a green photon, the anionic chromophore undergoes reprotonation by Glu222 and converts to the ground state of the neutral chromophore, thus completing wtGFP photocycle. Besides excited-state proton transfer (ESPT) responsible for the large

Stokes shift (LSS) (109 nm) in wtGFP, an additional phototransformation process triggered by violet light can occur. This phototransformation induces rearrangement of hydrogen bonds involved in the ESPT pathway, resulting in reduction of Stokes shift. The reduction of Stokes shift in wtGFP was discovered to be either reversible or irreversible depending on the intensity of illumination (Chattoraj et al., 1996; van Thor et al., 2002). The reversible photoswitching was proposed to occur because of a rotamer reorientation of the Thr203 side chain and *anti-syn* isomerization of Glu222, followed by a rearrangement of the hydrogen bond network to stabilize the anionic chromophore in the ground state. After relaxation in the dark, the side chains of Thr203 and Glu222 return to their initial conformations and the anionic chromophore is protonated by the Glu222 γ-carboxylate (Brejc et al., 1997; Palm et al., 1997). The irreversible photoswitching mechanism of wtGFP involves decarboxylation of Glu222 and subsequent chromophore deprotonation induced by hydrogen bond network rewiring (Bell et al., 2003; van Thor et al., 2002).

It was shown that ESPT is also responsible for LSS in red FPs, such as mKeima (Henderson et al., 2009b; Violot et al., 2009), LSSmOrange (Shcherbakova et al., 2012a) and LSSmKates (Piatkevich et al., 2010b). However, to date, there are no reports on a photoinducible reduction of Stokes shift in red FPs. In the course of directed molecular evolution of LSSmKate1 (Piatkevich et al., 2010a), we identified a mutant, which exhibited the photoinduced irreversible reduction of Stokes shift under violet illumination. This protein, named PSLSSmKate, in its initial state exhibits LSS of 177 nm and upon illumination with violet light photoconverts into a red FP with Stokes shift of 48 nm, which is typical for standard FPs. Here we report spectral, biochemical, and structural characterization of PSLSSmKate. Our data allow us to suggest a molecular mechanism of the irreversible photoswitching in PSLSSmKate. In addition, we demonstrate potential applications of PSLSSmKate in wide-field and superresolution fluorescence microscopy.

RESULTS

Characterization of Photoswitchable Derivative of LSSmKate1

During the screening for the LSSmKate variants (Piatkevich et al., 2010a; Piatkevich et al., 2010b) with improved photostability, we identified a clone that, along with decreasing red fluorescence when excited by blue light, exhibited substantial increase in fluorescence in a red channel (excitation 570/30 nm, emission 615/40 nm) upon illumination with 405 nm. Subsequent sequencing of the selected clone revealed two amino acid substitutions relative to LSSmKate1, namely, Tyr67Lys and Gly143Ser (here and below, the amino acid numbering follows that for LSSmKate1). According to the amino acid alignment, both introduced mutations are internal to the β-barrel protein fold (Figure S1 available online). We termed this mutant as *p*hotoswitchable *l*arge *S*tokes *s*hift *mKate* (PSLSSmKate).

Next, we conducted both in vitro and in-cell analysis of PSLSSmKate oligomeric state. In seminative polyacrylamide gel, PSLSSmKate ran as a monomer, even at a concentration as high as 1 mg/ml (Figure S2). The α-tubulin, β-actin, H3.2 histone, and CAAX fusion constructs incorporated well into the endogenous structures, indicating that PSLSSmKate exhibited monomeric behavior in mammalian cells (Figure S3).

Initially, PSLSSmKate matured into the LSS fluorescent form with excitation and emission peaks at 445 and 622 nm, respectively. In absorbance spectrum, the LSS form exhibited a single peak at 445 nm (Figure 1A). Illumination with 405 nm light of 90 mW/cm^2 resulted in appearance of an absorbance band with maximum at ~570 nm. It should be noted that absorbance of illuminated PSLSSmKate also revealed a band with a maximum at ~400 nm, which likely corresponds to the neutral GFP-like chromophore (Figure 1A). The red fluorescent form of photoswitched PSLSSmKate had excitation and emission maxima at 573 and 621 nm, respectively (Figure 1; Table 1). The LSS and red fluorescent forms of PSLSSmKate are characterized by molar extinction coefficients of 26,500 and 8,500 $M^{-1} \cdot cm^{-1}$ and fluorescence quantum yields at pH 7.4 of 0.21 and 0.16, respectively (Table 1). The LSS form of PSLSSmKate is 2.2-fold brighter than that of LSSmKate1. The apparent p*K*a values for the LSS and red forms are 6.5 and 8.2, respectively (Figure 1C). PSLSSmKate exhibited fast chromophore maturation at 37°C with a half-time of 90 min, which is similar to that of LSSmKate1 (Figure 1D).

To characterize the photoswitching properties of PSLSSmKate, we used wide-field epifluorescence microscopy of live HeLa cells expressing the untagged protein. Fluorescence of PSLSSmKate was evenly distributed in the cytosol and nucleus, without any aggregation (Figure S4). We used dark-to-red photoactivatable PATagRFP (Subach et al., 2010a) as a reference to compare photoswitching properties. First, we measured initial photoswitching rates under relatively high-intensity illumination (unless specifically stated, here and below, the light power is measured at a rear aperture of the 60× oil objective lens) at multiple wavelengths in the range of 330 to 500 nm (350/50 nm at 5.8 mW, 390/40 nm at 8.7 mW, 436/20 nm at 10.9 mW, and 480/40 nm at 16.7 mW). PSLSSmKate and PATagRFP had the similar spectral dependence of photoswitching rates. The most efficient photoactivation for both proteins was observed with 390/40 nm irradiation (Figure 1E). Photoswitching rates of PSLSSmKate using 436/20 nm and 480/40 nm light were about 6- and 12-fold lower, respectively, than that obtained with 390/40 nm light. This property allows selection of the appropriate filter set for imaging of the LSS form of PSLSSmKate without its photoswitching. At 390/40 nm illumination with 8.7 mW intensity, PSLSSmKate exhibited a 1.6-fold longer photoswitching half-time compared with PATagRFP (Figure 1F). The quantum yield of photoswitching for PSLSSmKate measured at 390/40 nm illumination was ~2×10^{-5}. To determine PSLSSmKate photostability, we performed photobleaching using 436/20 and 570/30 nm filters, which are optimal for excitation of the LSS and red forms, respectively. Normalized photostability of the LSS form was 2.0- and 1.4-fold lower than that of LSSmKate1 and LSSmKate2, respectively (Figure 1G). In turn, normalized photostability of the red form was 3.4- and 1.4-fold lower than that of mKate2 (Shcherbo et al., 2009) and PATagRFP, respectively (Figure 1H). Photobleaching of the photoswitched red form did not lead to increase of the LSS red fluorescence, indicating that photoswitching was irreversible (Figure S5) The red form of PSLSSmKate exhibited two-exponential photobleaching kinetics (Figure 1H).

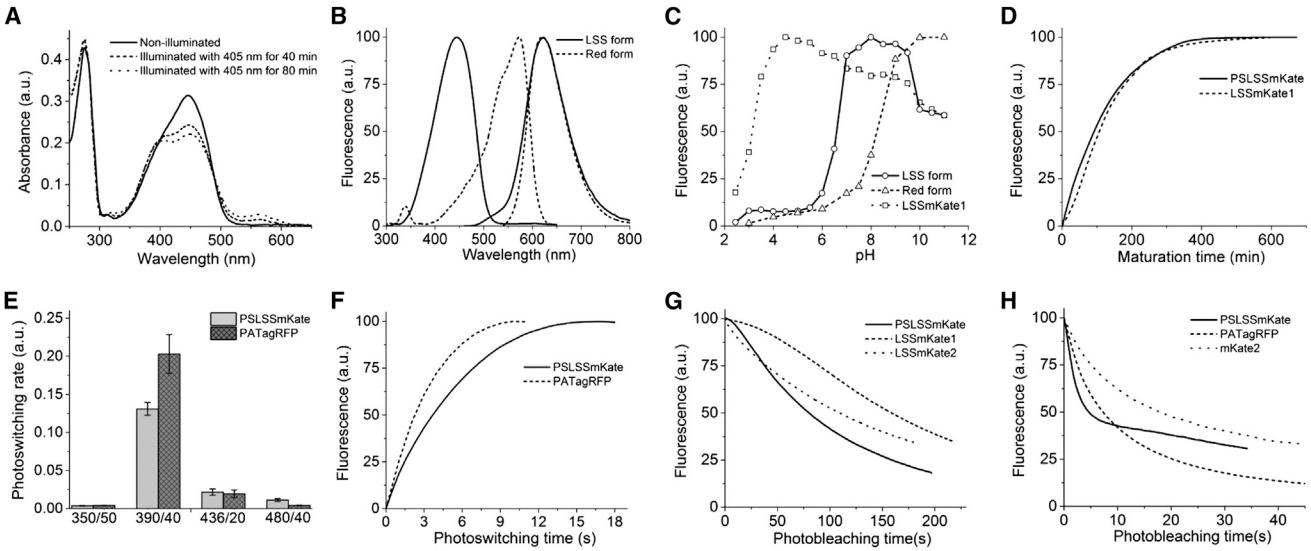

Figure 1. Spectral, Biochemical, and Photoswitching Characteristics of PSLSSmKate

(A) Absorbance spectra of purified PSLSSmKate before (solid line) and after illumination with 405 nm at 90 mW/cm^2 for 40 min (dashed line) and 80 min (dotted line).

(B) Fluorescence spectra of the LSS form (solid line) and the red form (dashed line) of purified PSLSSmKate in PBS buffer.

(C) Equilibrium pH dependence for the fluorescence of the LSS form (circles) and the red form (triangles) of purified PSLSSmKate and LSSmKate1 (squares).

(D) Fluorescence maturation kinetics for PSLSSmKate (solid line) and LSSmKate1 (dashed line) at 37°C in PBS buffer.

(E) Spectral dependence of the initial photoswitching rate for PSLSSmKate (solid columns) and PATagRFP (dashed columns) under 350/50 nm at 5.8 mW, 390/40 nm at 8.7 mW, 436/20 nm at 10.9 mW, and 480/40 nm at 16.7 mW. Error bars are the SEM.

(F) Time courses of the red forms of PSLSSmKate (solid line) and PATagRFP (dashed line) during illumination with 390/40 nm light at 8.7 mW.

(G) Photobleaching kinetics for the LSS form of PSLSSmKate (solid line), LSSmKate1 (dashed line), and LSSmKate2 (dotted line) under 436/20 nm illumination at 10.9 mW.

(H) Photobleaching kinetics for the red form of PSLSSmKate (solid line), PATagRFP (dashed line), and Kate2 (dotted line) under 570/30 nm illumination at 31.0 mW.

In (E)–(H), protein properties were measured in live HeLa cells using an Olympus IX81 inverted microscope equipped with 200 W metal-halide lamp and 60× oil objective lens. The light power was measured at a rear aperture of the objective lens. The photobleaching data (G and H) were normalized to the spectral output of excitation source, transmission profile of the excitation filter, and absorbance spectra of the proteins. See also Figures S1–S5.

Evaluation of PSLSSmKate as a Photoswitchable Fluorescent Probe

To demonstrate the applicability of PSLSSmKate as a photoswitchable fluorescent probe for wide-field microscopy, we fused it to histone 2B (H2B) and human cytochrome *c* oxidase subunit VIII and expressed in live HeLa cells. Two sets of filters allowed the visualization of both PSLSSmKate forms without any crosstalk between the channels. The fusion proteins underwent pronounced photoswitching by 390/40 nm light at 8.7 mW of wild-field microscope, giving the same distribution of the signals before and after the photoswitching (Figures 2A and 2B). A decrease in fluorescence of the LSS form was 3- to 10-fold, and an increase in fluorescence of the red form was 4- to 10-fold, resulting in up to 100-fold photoswitching contrast. The ability to image PSLSSmKate without its photoswitching, in addition to sufficient brightness and photostability of its LSS and red forms, allowed time-lapse imaging of intracellular dynamics of the tagged protein (Figure 2C). We also demonstrated that under the same imaging conditions, parental LSSmKate1 exhibited no photoswitching into the red form (Figure 2D).

Next, we evaluated the single-molecule characteristics of PSLSSmKate. We fused PSLSSmKate and PATagRFP to β-actin, expressed the constructs in HeLa cells, and imaged the live cells using photoactivated localization microscopy (PALM) under low levels of illumination with 405 nm photoswitching (from 0.1 to 10 W/cm^2) and high 561 nm excitation (1 kW/cm^2). The single-molecule statistics indicated that the photoswitched form of PSLSSmKate was comparably photostable, but less bright, and had higher localization uncertainty than PATagRFP (Figure 3). The photon statistics of the photoswitched PSLSSmKate molecules showed that they had properties sufficient for PALM imaging (Figure 4).

Crystal Structure of PSLSSmKate

To reveal a molecular mechanism responsible for the irreversible photoswitching of PSLSSmKate, we first determined the crystal structure of its LSS form at 2.7 Å resolution. Diffraction from the PSLSSmKate crystals is consistent with the space group I4 with unit cell dimensions $a = b = 99.03$ Å, $c = 106.61$ Å, and $\alpha = \beta = \gamma = 90°$. The overall structure of PSLSSmKate resembles that of GFP-like FPs. The crystal asymmetric unit contains two protein chains with the principal axes of each β-barrel at about 120° relative to each other. Electron density is well defined for residues 3 to 228 of the both subunits. Electron densities of the chromophores, autocatalytically formed from the Met63-Tyr64-Gly65 tripeptide, are consistent with that of the common DsRed-like chromophore (Figure S6). The electron density (especially in subunit B) slightly deviates from ideal shape and may indicate

Table 1. Spectral and Biochemical Properties of PSLSSmKate Compared with Parental LSSmKate1 and Other Selected Red FPs

Protein	mKate2	LSSmKate1	LSSmKate2	PATagRFP	PSLSSmKate	
					LSS Form	Red Form
Excitation maximum (nm)	588	463	460	562	445	573
Emission maximum (nm)	633	624	605	595	622	621
Extinction coefficient ($M^{-1} \cdot cm^{-1}$)	62,500[a]	31,200[b]	26,000[b]	66,000[c]	26,500	8,500
Quantum yield	0.40[a]	0.08[b]	0.17[b]	0.38[c]	0.21	0.16
Brightness	25,000	2,500	4,400	25,000	5,600	1,400
p*K*a	6.5[d]	3.2[b]	2.7[b]	5.3[c]	6.5	8.2
Photostability (s)	17	159	109	7	80	5
Maturation half-time at 37°C (min)	38[d]	100	150[b]	75[c]	90	NA
Half-time of photoswitching (s)	NA	NA	NA	2.3	3.7	

See also Figure S10. NA, not applicable.
[a]Data from Shcherbo et al. (2009).
[b]Data from Piatkevich et al. (2010a).
[c]Data from Subach et al. (2010a).
[d]Data from Chu et al. (2014).

traces of an immature chromophore, rather than of the alternative *trans* chromophore configuration. A *cis* configuration of the chromophore *p*-hydroxyphenyl ring predominates in both molecules in the asymmetric unit, but accurate assessment of the immature chromophore fraction is difficult at this resolution. The *cis* chromophores in both subunits exhibit significant deviations from the coplanarity between the hydroxyphenyl and imidazolinone rings. For the *cis* chromophore in the subunit A, the values of $\chi 1$ and $\chi 2$ torsion angles (i.e., around the $C\alpha = C\beta$ and $C\beta$-$C\gamma$ bonds of tyrosine) are 20.8° and −46.8°, respectively. For the *cis* chromophore of the subunit B, these angles are 28.0° and −70.5°, respectively.

We previously determined the crystal structure of LSSmKate1, the PSLSSmKate precursor (Piatkevich et al., 2010b). A superposition of the PSLSSmKate and LSSmKate1 structures resulted in a root-mean-square deviation of only 0.34 Å (1.03 Å) for C_α (all) atoms, which is at the level of overall coordinate error at this resolution. As expected from the fluorescence spectra of the LSS form, determination of the detailed structure of PSLSSmKate revealed a proton relay similar to that found in LSSmKate1 (Piatkevich et al., 2010b). Namely, in both independent PSLSSmKate molecules, the hydroxyphenyl group of the chromophore forms a hydrogen bond with the carboxyl group of Glu160, which is in turn hydrogen bonded to Ser143, Ser158, and a water molecule (Figure 5A). Furthermore, the geometry of the hydrogen bonds formed by the hydroxyphenyl group of the chromophore and the Glu160 side chain in both PSLSSmKate and LSSmKate1 structures were practically superimposable with each other (Figure 5B).

Further pairwise comparisons of the immediate chromophore environment of PSLSSmKate with that of LSSmKate1 revealed substantial differences in the hydrogen bond networks involving the Arg197 and Glu215 side chains. First, the Glu215 side chains in PSLSSmKate and LSSmKate1 occupy different conformations: their carboxylate functionalities lie in orthogonal planes in case A chains, and in case of B chains, the angle between these plains is notably less than 90°. In both subunits of PSLSSmKate, the carboxylate of Glu215 forms a hydrogen bond with the N3 atom of 5-imidazolinone ring of the chromophore and is not involved in interactions with the side chain of Arg197. In contrast, the Glu215 residue in all four subunits of the LSSmKate1 structure forms a hydrogen bond with the guanidine group of Arg197 (Figure 5C). Moreover, in A and D subunits of LSSmKate1, the oxygen atom of the Glu215 carboxylate locates more than 4.0 Å away from the N3 atom 5-imidazolinone ring of the chromophore, meaning that formation of hydrogen bond between Glu215 and the chromophore is not possible. Second, the side chains of Arg197 in the PSLSSmKate and LSSmKate1 structures are located differently with respect to the chromophore. The Arg197 guanidine group in PSLSSmKate is oriented toward Ser148 and Ser165 and is involved in hydrogen bond interactions with them. In LSSmKate1, the Arg197 side chain is located 3.8 Å above the methylidene bridge of the chromophore (when the subunit is viewed with N and C termini upward) and participates in hydrogen bond interactions with Glu215 and the hydroxyl group of Tyr67 (Figure 5D).

Mass-Spectral Analysis of PSLSSmKate

Nearly all irreversible photoswitching occurring in GFP-like FPs are accompanied by chemical transformation of either the chromophore or amino acid side chain functionalities near the chromophore. To define chemical modifications occurring in PSLSSmKate upon photoswitching, we performed mass spectrometry (MS) analysis of its LSS and red forms. The mass spectrum of the PSLSSmKate trypsin-digested fragments before photoswitching revealed a monoisotopic mass of 2,215.1 Da, corresponding to the peptide Ile202-Arg220 (Figure S7A). In the mass spectrum of photoswitched PSLSSmKate, we observed a new monoisotopic mass of 2,171.1 Da, which is 44 Da less than the mass of the fragment before illumination (Figure S7B). The mass decrease and the MS/MS analysis of the 2,171.1 peak revealed decarboxylation of Glu215.

Mutagenesis and Spectroscopic Analysis of PSLSSmKate

To examine contributions of the residues interacting with the chromophore to the photochemical properties of PSLSSmKate,

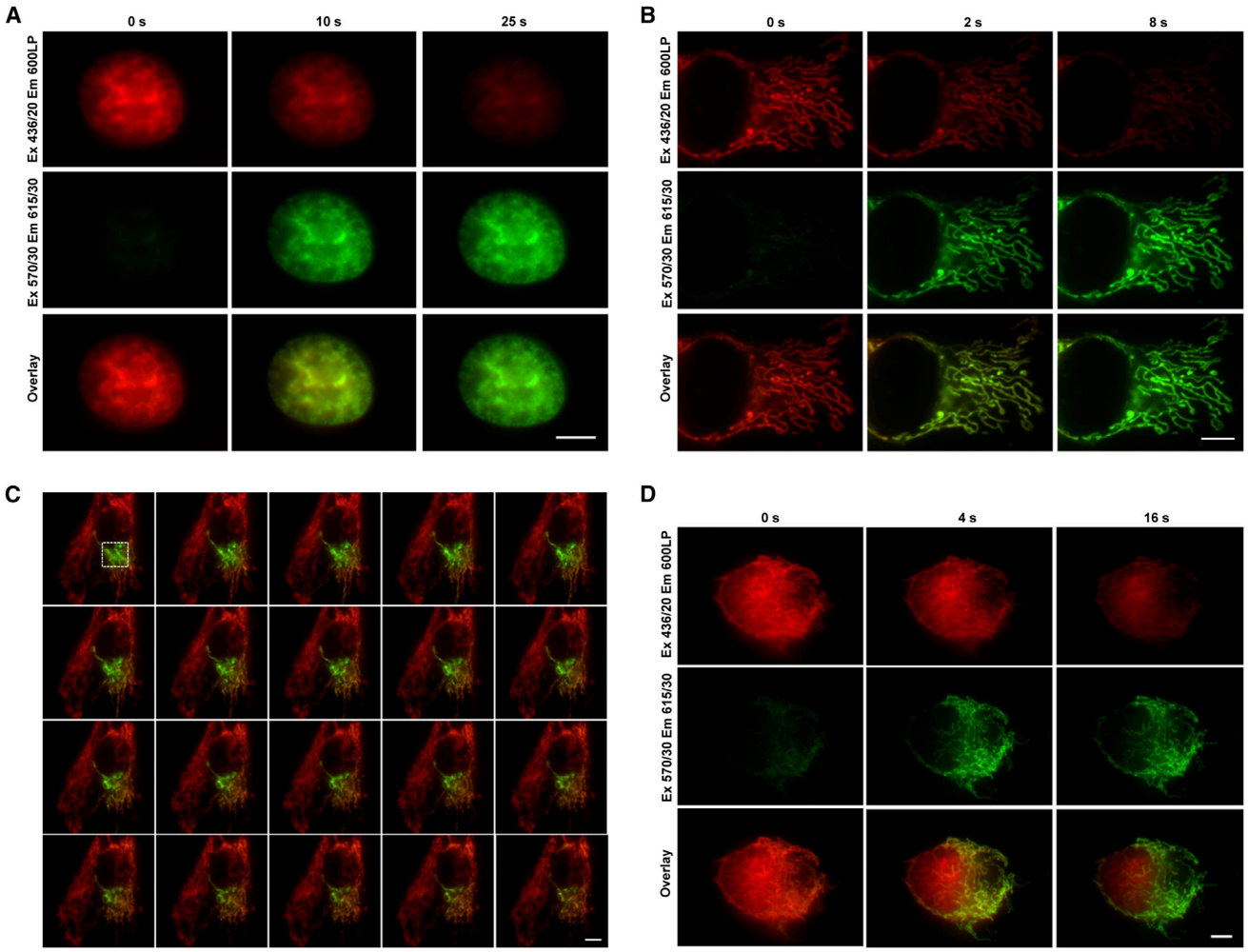

Figure 2. Epifluorescence Imaging of PSLSSmKate Fusions in Live HeLa Cells

(A and B) Cells expressing (A) H2B-PSLSSmKate fusion localized in a nucleus and (B) PSLSSmKate fused to human cytochrome *c* oxidase subunit VIII localized in mitochondria. Photoswitching was performed using 390/40 nm light at 8.7 mW for the indicated time.

(C) Series of still fluorescent images captured with 1 min interval showing dynamics of the PSLSSmKate fusion in mitochondria. Photoswitching was performed using the 390/40 nm light at 8.7 mW for 6 s. The area of the PSLSSmKate photoswitching is indicated with a white box.

(D) Cells coexpressing the H2B-LSSmKate1 fusion and PSLSSmKate fused to human cytochrome *c* oxidase subunit VIII. Photoswitching was performed by 390/40 nm light for the indicated time. Scale bar represents 10 μm.

we introduced five single-point mutations into PSLSSmKate: Lys67Tyr, Ser143Gly, Ser158Ala, Glu160Ala, and Arg197Tyr. The Glu215 residue is highly conserved among all GFP-like FPs, and its substitution strongly impairs chromophore maturation (Subach et al., 2010b). Therefore, it was not selected for mutagenesis. The side chain of Ala is not capable of hydrogen bond formation, and in contrast to the guanidine group of Arg, the Tyr *p*-hydroxyphenyl group cannot support multiple hydrogen bonds. We reasoned that the introduced mutations most likely would interrupt the hydrogen bond network in the vicinity of the chromophore.

The spectral and photochemical characteristics of the PSLSSmKate mutants were measured at pH 7.4. The Lys67Tyr substitution caused 21 nm red shift of the excitation spectrum of PSLSSmKate but did not affect its emission maximum. The Ser143Gly mutation increased quantum yield by ~50% and blue-shifted the emission maximum by 33 nm while leaving the excitation maximum unchanged. This blue shift in emission can be explained by a chromophore isomerization from the *cis* to *trans* configuration, as it was observed for LSSmKate2 (Piatkevich et al., 2010b). Both Lys67Tyr and Ser143Gly substitution caused appearance of a shoulder at ~530 nm in the emission spectrum. The PSLSSmKate/Ser158Ala variant had the increased quantum yield and demonstrated a 13 nm red shift in excitation. The PSLSSmKate/Glu160Ala variant exhibited an excitation maximum red-shifted by 112 nm, while its emission maximum remained unchanged. This observation indicates that Glu160Ala substitution altered the PSLSSmKate chromophore from neutral to anionic state. Quantum yield of the anionic chromophore in the Glu160Ala mutant increased by ~50% comparing with the neutral chromophore in PSLSSmKate. Interestingly, the Arg197Tyr mutant appeared to be almost

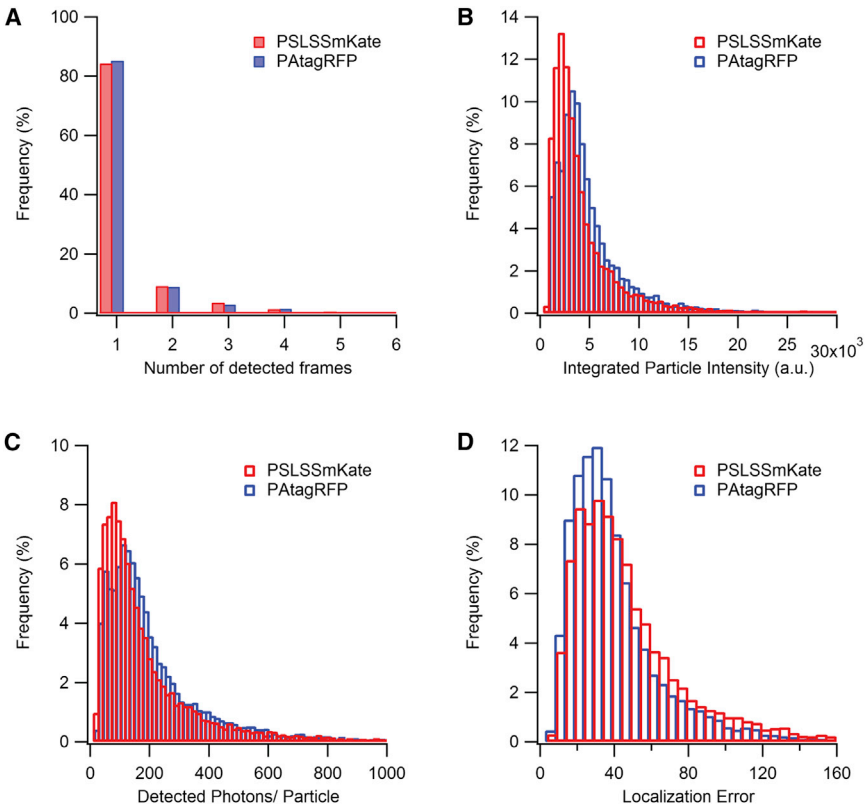

Figure 3. PALM Single-Molecule Analysis of PSLSSmKate and PATagRFP Fusions with β-Actin in Live HeLa Cells

Five thousand consecutive frames of both PSLSSmKate-β-actin and PATagRFP-β-actin were recorded on the same day under identical illumination conditions. Both fluorophores were photoconverted using low-power continuous 405 nm laser excitation.

(A) Histogram of the fluorescence lifetime of the number of frames a single molecule was detected in 0.03 s images of PSLSSmKate (red) and PATagRFP (blue).

(B) Distribution of the total integrated particle intensity for PSLSSmKate (mean 4,702, median 2,749) and PATagRFP (mean 5,422, median 3,553).

(C) Distribution of the total number of photons from PSLSSmKate (mean 226, median 122) and PATagRFP (mean 251, median 150).

(D and B) Distribution of the localization error for PSLSSmKate (mean 46.1, median 35.9) and PATagRFP (mean 38.5, median 30.7).

nonfluorescent: its quantum yield was ~0.007. The fluorescence spectra of all generated mutants are shown in Figure S8, and their spectroscopic properties are summarized in Table 2.

Next, we recorded changes in red fluorescence of PSLSSmKate, its point mutants, and LSSmKate1 excited by 445 and 560 nm light under continuous 90 mW/cm^2 illumination with 405 nm. All proteins exhibited the decrease in LSS red fluorescence (Figure S9A). However, a substantial increase in red fluorescence excited at 560 nm was observed for PSLSSmKate only (Figure S9B). A small increase (<5-fold) in red fluorescence excited at 560 nm was observed for the Ser143Gly mutant. Thus, the interruption of the hydrogen bond network in an immediate chromophore environment resulted in the complete loss of either photoswitching or fluorescence (in the case of the Arg197Tyr mutant) in PSLSSmKate.

DISCUSSION

Spectral and Biochemical Properties of PSLSSmKate

Previously, we determined the crystal structure of LSSmKate1 at the resolution of 2.0 Å and revealed relationships between the LSSmKate1 structure and its spectral properties (Piatkevich et al., 2010b). Here we performed comparison of the spectral, biochemical, and structural properties of PSLSSmKate and LSSmKate1. We have identified two amino acid substitutions in PSLSSmKate, such as Tyr68Lys and Gly143Ser, compared with parental LSSmKate1 (Figure S1). The introduced mutations were internal to the β-can protein fold and did not alter the monomeric state of parental LSSmKate1 as confirmed by in vitro analysis and microscopy (Figures S2–S4). An efficiency of chromophore maturation was not affected by the mutations too: PSLSSmKate and LSSmKate1 exhibited similar kinetics of the chromophore formation and extinction coefficients (Figure 1D and Table 1).

The introduced mutations had a minor effect on the fluorescence spectrum of LSSmKate1 (Figure S10). The excitation maximum of the LSS form of PSLSSmKate exhibited a blue shift of 18 nm relative to LSSmKate1, while their emission maxima were almost the same (Table 1). It is known that changes in charge distribution in an immediate chromophore environment can affect FP spectral properties (Shu et al., 2006). Interactions between the chromophore and its environment that stabilize chromophore charge tend to increase energy barrier for charge transfer resulting in a hypsochromic shift of absorbance and fluorescence (Ai et al., 2008b; Chica et al., 2010; Piatkevich et al., 2013). The major differences in the immediate chromophore environments of PSLSSmKate and LSSmKate1 occur at positions Arg197 and Glu215 (Figure 5C). In contrast to LSSmKate1, the side chain of Glu215 is within a hydrogen-bonding distance to the imidazolinone ring nitrogen, suggesting that Glu215 is protonated. In the case of LSSmKate1, the Glu215 side chain forms a hydrogen bond with the guanidinium group of Arg197, suggesting that Glu215 is deprotonated. In the structure of PSLSSmKate, the side chain of Arg197, which appears to be charged throughout the physiological pH range, is oriented away from the hydroxyphenyl group of the chromophore, while in LSSmKate1, the Arg197 guanidinium group is located exactly above the methylidene bridge of the chromophore (Figures 5C and 5D). Therefore, we propose that the arrangement of the Arg197 and Glu215 side chains is responsible for the blue shift of the PSLSSmKate excitation relative to that of LSSmKate1.

Further analysis of the PSLSSmKate structure revealed a proton relay between the chromophore hydroxyl group and Glu160, similar to that in LSSmKate1 (Figure 5B). It was shown that a

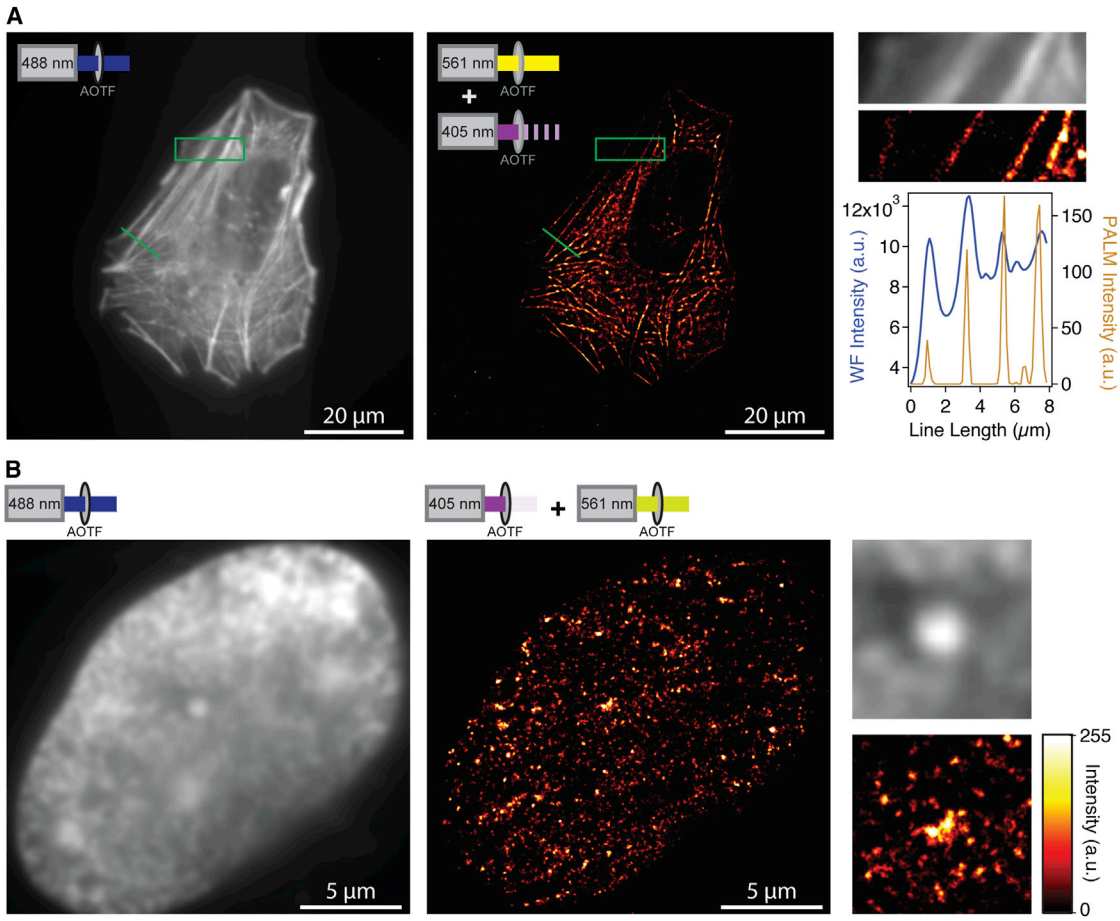

Figure 4. PALM Imaging of PSLSSmKate Fusions with β-Actin and H2B in Live U2OS Cells

(A) Right: averaged wide-field (WF) image of 1,000 consecutive frames of unconverted PSLSSmKate-β-actin, excited by a 488 nm laser. Middle: PALM image of 10,000 consecutive frames of photoswitched PSLSSmKate-β-actin of the same cell as on the right. PSLSSmKate is photoswitched by millisecond pulses of a 405 nm laser, which strobes twice a second, and is detected via 561 nm laser excitation. The 236,355 detected particles are displayed according their localization precision determined by a full width at half maximum (FWHM). The mean localization error was 47.9 nm. The particles are color-coded according to their fluorescence intensity. Left: magnified image of the region specified by the green rectangle and an intensity line scan of the green line for both WF and PALM images. The line scan highlights the 4-fold improvement in resolution by PALM imaging of PSLSSmKate.

(B) Right: averaged intensity image of 100 consecutive frames of unconverted H2B-PSLSSmKate within a nucleus, excited by a 488 nm laser. Middle: PALM image of 10,000 consecutive frames of H2B-PSLSSmKate, which was photoconverted using low-power continuous 405 nm laser excitation. The 89,217 detected particles are displayed according their localization using FWHM. The mean localization error was 46.2 nm. Left: magnified images of the center region. PALM imaging of PSLSSmKate reveals fine structure in the H2B distribution within a nucleus. All images were recorded at a frame rate of 20 frames/s.

hydrogen bond between the LSSmKate1 chromophore and the carboxylic group of Glu160 serves as the proton pathway for ESPT (Piatkevich et al., 2010b; Randino et al., 2012; Zhang et al., 2011). When excited by blue light, the neutral (protonated) state of the chromophore undergoes proton transfer to its nearest environment, thus, converting into an excited state of the anionic (deprotonated) chromophore. Subsequently, the excited anionic chromophore emits red fluorescence and decays to the ground anionic chromophore, which undergoes protonation to complete the photocycle. The similar chromophore photocycles involving ESPT were proposed for other LSS FPs, such as green T-Sapphire (Zapata-Hommer and Griesbeck, 2003), yellow mAmetrine (Ai et al., 2008a), orange LSSmOrange (Shcherbakova et al., 2012a) and red mKeima (Henderson et al., 2009b). We suggest that the proton relay revealed in PSLSSmKate enables ESPT and is responsible for the large Stokes shifted red fluorescence of its nonphotoswitched form.

Interestingly, the p*K*a value of red fluorescence of nonphotoswitched PSLSSmKate is shifted by more than 3 units toward an alkaline pH compared with that of LSSmKate1 (Figure 1C). Based on pH-dependent spectral changes of LSSmKate1, we previously assigned the apparent p*K*a value of its fluorescence to the direct titration of the Glu160 carboxylate group (Piatkevich et al., 2010b). Indeed, the protonation of Glu160, acting as a proton acceptor, disables ESPT and, therefore, diminishes LSS fluorescence. We propose that the same mechanism of fluorescence quenching upon decreasing pH takes place in PSLSSmKate. The substantial difference in the p*K*a values of fluorescence can be explained by an elevation of the p*K*a value of the Glu160 side chain in PSLSSmKate due to the formation of

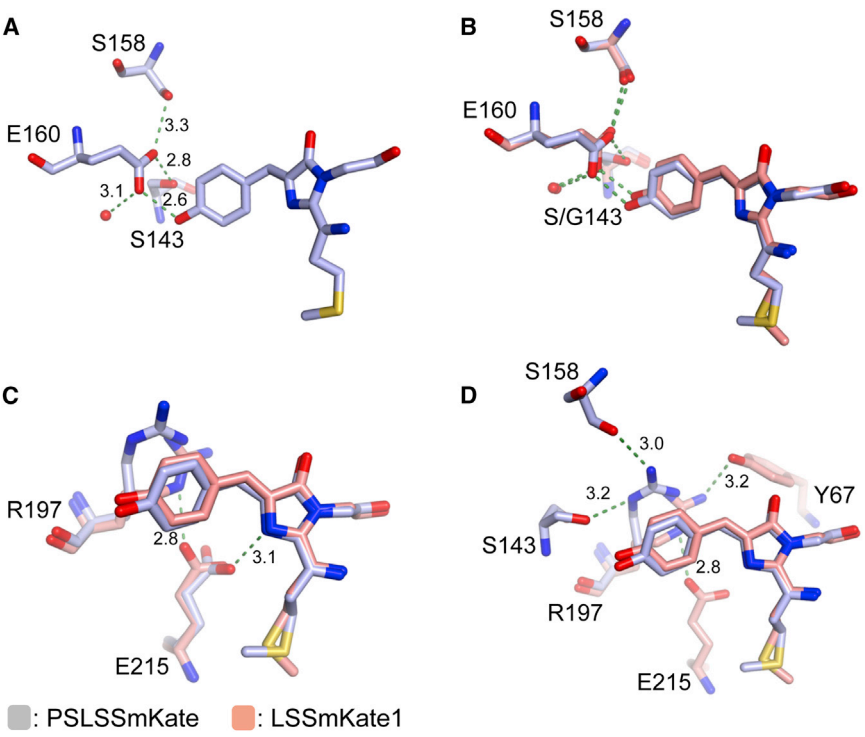

Figure 5. Structural Comparison of PSLSSmKate and LSSmKate1

(A) Molecular structure of the PSLSSmKate chromophore and selected residues in its vicinity are shown.

(B–D) Superpositions of the PSLSSmKate chromophore with the LSSmKate1 (PDB accession number 3NT9) chromophore and selected residues in the vicinity of the chromophores are shown. Hydrogen bonds are represented as dashed green lines with the lengths indicated in angstroms, atoms are colored by atom type, and water molecules are shown as red spheres. See also Figures S6 and S7 and Table S1.

an additional hydrogen bond with Ser143, which, in turn, is hydrogen bonded to Arg197 (Figures 5B and 5D). Notably, it is well appreciated that p*K*a values for Glu side chains buried into protein interior can range from 5.2 to 9.4, depending on local environment (Isom et al., 2010). It is should be also noted that under the crystallization conditions used (pH 3.5), the LSSmKate1 chromophore is more coplanar than that of PSLSSmKate: the values of $\chi 1$ and $\chi 2$ torsion angles are $6 \pm 5^\circ$ and $-19 \pm 5^\circ$ versus 20.8° and -46.8° in the A subunit and 28.0° and -70.5° in the B subunit of PSLSSmKate. Quantum yield of FPs depends on coplanarity of a chromophore (Shu et al., 2006). At the pH of the buffer used for crystallization, PSLSSmKate is nonfluorescent, while LSSmKate1 exhibits maximal brightness (Figure 1C). This suggests that low pH can cause the chromophore deformation and decrease in fluorescence.

PSLSSmKate for Live-Cell Imaging

We examined the performance of PSLSSmKate as an optical probe in live cells using epifluorescence microscopy and superresolution PALM. Because of the monomeric state, the fusions of PSLSSmKate to β-actin and α-tubulin localized correctly, demonstrating its usefulness as a fusion tag (Figures S3A and S3B). Despite the limited brightness of PSLSSmKate compared with other photoswitchable red FPs (the brightness of the PSLSSmKate initial and photoswitched forms were ~22% and ~5.4% of that of PATagRFP, respectively), it was sufficient to image tagged proteins and track their dynamics (Figure 2). Furthermore, single-molecule characterization indicated that PSLSSmKate can be used in PALM imaging, although its performance in superresolution microscopy was lower compared to PATagRFP (Figures 3 and 4).

Interestingly, nonphotoswitched PSLSSmKate can be imaged with diffraction-limited resolution using blue excitation light without changing the emission optics. This property of PSLSSmKate, when combined with a 405/436/561 nm triple-band dichroic, allows monitoring both nonphotoswitched and photoswitched species in the same cell without changing the emission path simply by switching the laser excitation. Because lasers can be switched on and off in microseconds, it would be possible to detect both PSLSSmKate states with high temporal resolution and with an optical setup that does not require moving parts, allowing a simplified and stable setup for pulse-chase cell experiments.

Another possibility would be to use PSLSSmKate simultaneously with other PSFPs to label up to four intracellular protein populations. This complementing PSFP should have spectrally distinct excitation spectra in both states as well as an independent photoswitching light. Recently reported photoswitchable from orange to far-red PSmOrange (Subach et al., 2011b) and PSmOrange2 (Subach et al., 2012) proteins could satisfy these requirements. The original orange and photoswitched far-red states should be spectrally resolvable with those of PSLSSmKate. Moreover, PSmOrange and PSmOrange2 are photoswitched with blue-green light, not violet as required for the PSLSSmKate photoconversion.

Molecular Mechanism of PSLSSmKate Photoswitching

Excitation spectra of the LSS and red forms of PSLSSmKate exhibit bands with the maxima at 445 and 573 nm, respectively (Figure 1B; Table 1). The band at 445 nm is characteristic for the neutral DsRed-like chromophore, while the band at 573 nm in the red form can be attributed to the anionic form of DsRed-like chromophore (Henderson et al., 2009b; Piatkevich et al., 2010b; Violot et al., 2009). The band at 400 nm revealed in absorbance spectrum of photoconverted PSLSSmKate corresponds to the neutral GFP-like chromophore (Figure 1A). This is in agreement with the crystallographic data indicating traces of the immature chromophore in PSLSSmKate. Absorbance spectra also demonstrated that the band at 400 nm did not undergo any noticeable changes upon illumination with 405 nm. This observation indicates that the GFP-like chromophore was not photoactive and did not participate in photoswitching into the red form. Thus, according to the spectroscopic data, the

Table 2. Spectroscopic Properties for the PSLSSmKate Single-Point Mutants

Mutation in PSLSSmKate	Excitation/ Emission Maxima (nm)	Extinction Coefficient ($M^{-1} \cdot cm^{-1}$)	Quantum Yield
None	445/622	26,500	0.21
K67Y	466/623	ND	0.18
S143G	447/589	ND	0.30
S158A	458/624	29,100	0.28
E160A	557/622	45,200	0.30
R197Y	460/594	34,400	0.007

See also Figures S8 and S9. ND, not determined.

photoswitching of PSLSSmKate is accompanied by an irreversible transition of the DsRed-like chromophore from the neutral state to the anionic state.

The chromophore deprotonation can occur as a consequence of the photochemical reaction, inducing rearrangements of the hydrogen bonds between the chromophore and its immediate environment. Indeed, MS data of the Ile202-Arg220 peptide indicates the loss of 44 Da upon photoswitching, which corresponds to the decarboxylation of Glu215 (Figure S7). The Glu215 decarboxylation can be explained in terms of the Kolbe-type radical mechanism. It was shown that the imidazolinone ring of the neutral GFP-like chromophore is electron deficient (Bublitz et al., 1998; Chattoraj et al., 1996) and therefore can act as an oxidant (Bell et al., 2003; van Thor et al., 2002). In the crystal structure of PSLSSmKate, the N3 atom of the chromophore imidazolinone ring forms a hydrogen bond with the Glu215 carboxyl group (Figure 5C). We propose that upon excitation of the chromophore, this hydrogen bond allows direct and efficient electron withdrawing from the carboxyl group of Glu215 to the imidazolinone ring, resulting in a formation of the γ-carboxyl radical of Glu215. This radical is highly unstable and undergoes rapid decarboxylation with subsequent retrotransfer of electron and proton. Thus, the decarboxylation of Glu215 would result in elimination of the hydrogen bond with the chromophore. Because after Glu215 decarboxylation, the electron lone pair of the N3 atom no longer participates in the hydrogen bond formation, it may cause redistribution of electron density within the chromophore π-conjugated system. Most likely the increase of electron density at N3 of the imidazolinone ring would lower the p*K*a of the chromophore, followed by chromophore deprotonation and subsequent rearrangements of the hydrogen bonds around the *p*-hydroxyphenyl moiety of the chromophore. The anionic chromophore can be stabilized by Ser143. The side chain of Ser143 locates only 3.5 Å away from the oxygen atom of the *p*-hydroxyphenyl moiety. Slight rotation around the C_α-C_β bond of Ser143 can bring its hydroxyl group close enough to the phenolate oxygen to form a moderate hydrogen bond (2.5–3.2 Å) to stabilize the anionic chromophore (Jeffrey, 1997).

On the basis of the described mechanism, we propose a simplified scheme for the photochemical transformation occurring upon the PSLSSmKate photoswitching, involving a Koble-type reaction mechanism for the Glu215 decarboxylation (Figure 6). On the basis of the detailed comparison of PSLSSmKate and LSSmKate1 crystal structures, we propose that an exact location of Arg197 plays the critical role for photoswitching. Hydrogen bond interaction between Arg197 and Glu215 observed in all subunits of the LSSmKate1 structure significantly increases electron density at the Glu215 carboxylic group. As a result, the Kolbe-type decarboxylation of Glu215 in LSSmKate1 becomes impossible because of insufficient withdrawing of electron density from Glu215 during transition of the chromophore into an excited state.

The wavelength dependence of the photoswitching is also in agreement with the proposed Kolbe-type mechanism of decarboxylation. Previously, it was shown that an oxidizing power of the chromophore excited state controls the rate of the decarboxylation reaction in GFP (Bell et al., 2003). The S2 (or higher) excited state of the chromophore is more powerful oxidizer than the S1 excited state, enabling the higher rates of decarboxylation. Typically, a second absorption singlet band S2–S0 for the DsRed-like chromophore is centered at about 360 to 390 nm. In the case of PSLSSmKate, 390/40 nm illumination populates the S2 (or higher) excited state with the higher probability than illumination with 436/20 or 480/40 nm, resulting in the higher efficiency of photoswitching. The quantum yield of photoswitching for PSLSSmKate is similar to that of other PAFPs and PSFPs (Thompson et al., 2010).

The suggested photoswitching mechanism is in an agreement with the mutagenesis data. The Lys67Tyr substitution completely disables the PSLSSmKate photoswitching (Figure S9). The replacement of Lys67 with Tyr can cause relocation of Arg197 closer to the Glu215 side chain, so that hydrogen bond formation between Agr197 and Glu215 becomes possible. As discussed above, this hydrogen bond disables the Glu215 decarboxylation. Previously we proposed that positions 67 and 197 in red FPs are the key positions for the photoswitchable and photoactivatable phenotypes (Subach et al., 2011a). The results reported here help to understand the role of amino acid residues in the 67 and 197 positions in more details.

The Ser143Gly mutation changes configuration of the chromophore from *cis* to *trans*, as can be suggested from fluorescence spectrum of the PSLSSmKate/Ser143Gly mutant. Although PSLSSmKate/Ser143Gly still exhibits the photoswitching ability, its efficiency is low: an increase in the brightness of the red form is <5-fold (Figure S8). In turn, the Ser158Ala mutation completely disables the PSLSSmKate photoswitching (Figure S8). We suggest that Ser158 is required for a stabilization of the negative charge on Glu160. Replacement of Ser158 with Ala prevents formation of the hydrogen bond between Ser143 and the chromophore as energetically unfavorable, possibly because of the formation of two negatively charged groups in close proximity to each other (i.e., the carboxylic group of Glu160 and the phenolic group of the chromophore). The results obtained for the Ser143Gly and Ser158Ala variants suggest that hydrogen bond interactions involving the hydroxyphenyl group of the chromophore also play crucial role in PSLSSmKate photoswitching. The most likely Ser143 and Ser158 stabilize the anionic form of the chromophore in the photoconverted state. In the case of the Arg197Tyr mutant, we did not observe any increase in red fluorescence upon illumination. However, we cannot determine whether this was due to low quantum yield of the photoswitched product or to disabled photoconversion. However, this mutation showed that Arg197 plays a crucial role for the fluorescent properties of PSLSSmKate.

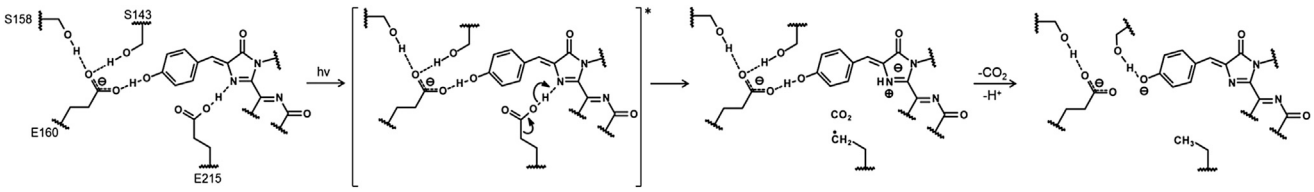

Figure 6. Scheme of Photochemical Transformation of PSLSSmKate
The hydrogen bonds are shown with dashed lines. The chromophore in the excited state is denoted with an asterisk. *hv*, illumination with violet light. A migration of the electron density is shown with the curved arrows.

A similar mechanism of photoswitching was previously reported for the photoactivatable GFP variant, PAGFP. The light-induced decarboxylation of the Glu222 residue (corresponds to Glu215 in PSLSSmKate) is followed by the rearrangement of the hydrogen bond network around the GFP-like chromophore that results in a formation of the anionic chromophore (Henderson et al., 2009a). The Kolbe-type reaction mechanism of the photoinduced Glu decarboxylation was also shown to occur in the wtGFP (Bell et al., 2003; van Thor et al., 2002), DsRed (Habuchi et al., 2005), PAmCherry (Subach et al., 2009), and PATagRFP (Subach et al., 2010a).

SIGNIFICANCE

PSLSSmKate represents the photoswitchable phenotype thst was not observed in red FPs. We have determined the crystal structure of PSLSSmKate, analyzed its photochemical transformation using MS, and performed a mutagenesis analysis, which can guide future design and improvement of LSS FPs of this phenotype. We propose a molecular mechanism for PSLSSmKate irreversible photoswitching, which is unique for red FPs. Because of its monomeric state and the sufficient photostability of the photoconverted form, PSLSSmKate is a useful variant to engineer advanced photoswitchable LSS red probes for wide-field and PALM fluorescence imaging. Our results may also facilitate the design of photoswitchable LSS FPs of other colors using green T-Sapphire (Zapata-Hommer and Griesbeck, 2003), yellow mAmetrine (Ai et al., 2008a), and orange LSSmOrange (Shcherbakova et al., 2012a) as initial LSS FP templates.

EXPERIMENTAL PROCEDURES

Mutagenesis and In Vitro Protein Characterization

Site-specific mutations were introduced using the QuikChange Mutagenesis kit (Stratagene). After mutagenesis, a pool of mutants, cloned into a pBAD/His-B vector (Invitrogen), modified by shortening the N-terminal polyhistidine tag to the MGSHHHHHHGRS- amino acid sequence, was electroporated into the *E. coli* bacterial host LMG194 (Invitrogen) and grown overnight on Luria broth (LB)/agar/ampicillin Petri dishes supplemented with 0.02% (w/v) L-arabinose at 37°C. For spectroscopic studies, colonies of interest were cultured overnight in 100 ml of LB or RM minimal medium/ampicillin supplemented with 0.01% (w/v) L-arabinose to induce protein expression and purified with nickel nitrilotriacetic acid (Ni-NTA) agarose (Qiagen). Excitation and emission spectra were measured with a FluoroMax-3 spectrofluorometer (Jobin Yvon) or SpectraMax M2e plate reader (Molecular Devices). For absorbance measurements, a Hitachi U-2000 spectrophotometer was used.

Protein maturation measurements were performed as described previously (Piatkevich et al., 2010a; Subach et al., 2010a). In brief, LMG194 bacterial cells were grown at 37°C overnight in LB medium supplemented with ampicillin. The next morning, cells were diluted to optical density 1.0 at 600 nm, and 0.02% arabinose was added. After 1 hr, the cultures, each 100 ml total volume, were harvested and the proteins were purified using Ni-NTA agarose within 30 to 40 min with all procedures and buffers at or below 4°C. Protein maturation was performed at 37°C in 0.5 ml of the 50 mM NaH_2PO_4, 300 mM NaCl, 5 mM β-mercaptoethanol buffer at pH 8.0 and followed by fluorescence with a FluoroMax-3 spectrofluorometer. The fluorescence value at time zero was subtracted from each subsequently measured fluorescent signal.

To determine extinction coefficients, we relied on measuring the mature chromophore concentrations, using alkali-denatured proteins. It is known that extinction coefficient of synthetic tyrosine-containing GFP-like chromophores is 44,000 $M^{-1} \cdot cm^{-1}$ at 447 nm in 1 M NaOH. On the basis of the absorbance of the native and denatured proteins, molar extinction coefficients for the native states were calculated.

For determination of the quantum yields, the fluorescence of PSLSSmKate and its mutants was compared with equally absorbing mKeima (quantum yield 0.24). pH titrations were performed using a series of buffers (100 mM NaOAc, 300 mM NaCl for pH 2.5–5.0, and 100 mM NaH_2PO_4, 300 mM NaCl for pH 4.5–9.0).

For photoswitching of PSLSSmKate, its mutants and LSSmKate1 in solution at concentration of 1 mg/ml, a custom-made 405 nm array consisting of 3 × 5W LZ1 light-emitting diodes (LEDEngin) assembled with 20° reflectors was used. Intensity of 405 nm light used for photoswitching was 90 mW/cm^2. Concentration of the proteins was determined using BCA Protein Assay Kit (Pierce).

Construction of Mammalian Plasmids

To construct pPSLSSmKate-N1 and pH2B-PSLSSmKate-N1 plasmids, gene of PSLSSmKate was PCR amplified as *Age*I-*Not*I fragment and swapped with enhanced GFP (EGFP) gene in pEGFP-N1 and pH2B-EGFP-N1 vectors (Clontech). To generate PSLSSmKate-CAAX fusion protein, a PCR-amplified BamHI/*EcoRI* fragment encoding gene of PSLSSmKate with Kozak sequence was swapped with mCherry gene in pcDNA3.1-mCherry-CAAX vector (gift of Jacco van Rheenen). To prepare pPSLSSmKate-β-actin-C1, pPSLSSmKate-α-tubulin and pPSLSSmKate-H3.1-C1, the PSLSSmKate gene was PCR amplified as *Nhe*I-BglII fragment and swapped with EGFP in pEGFP-α-actin-C1 (Clontech), pEGFP-α-tubulin-C1 (Clontech) and pEGFP-H3.1-C1 (gift of Jeffrey Segall), respectively.

Fluorescence Microscopy and Cell Imaging

HeLa, Cos-7, U2OS, and MTLn3 cells were grown on 23 mm glass-bottom dishes (MatTek) in minimum essential medium (HyClone) supplemented with 10% or 5% (in the case of MTLn3) fetal bovine serum (BenchMark). Transfection was performed with Effectene (Qiagen). Wide-field imaging of live cells was performed 48 to 72 hr after transfection. Cells were imaged using the Olympus IX81 inverted microscope equipped with 60× and 100× oil objective lens, a 200 W metal-halide lamp, a 390/40 nm exciter for photoswitching, and two filter sets 436/20 nm exciter, 600 nm LP emitter, and 570/30 nm exciter, 615/40 nm emitter (Chroma) to acquire red fluorescence of initial and photoswitched forms of PSLSSmKate. Quantum yield of photoswitching was measured in HeLa cells expressing nontargeted PSLSSmKate using 60× oil immersion objective lens and 390/40 nm exciter for photoswitching and calculated according to the method described previously (Matsuda et al., 2008). For photobleaching experiments with the LSS form of PSLSSmKate and LSSmKates expressed in cells, the 60× oil objective and the filter set

436/20 nm exciter, 600 nm LP emitter (Chroma) were used. For photobleaching experiments with the red form of PSLSSmKate, PATagRFP and mKate2 expressed in HeLa cells, the 60× oil objective and the filter set 570/30 nm exciter, 615/40 nm emitter (Chroma) were used.

All live-cell PALM imaging was performed at 37°C. Cells were grown and imaged in DMEM without phenol red (Invitrogen) with 10% fetal bovine serum on precleaned coverslips. The comparison live-cell PALM data sets were recorded on a Nikon Ti-Eclipse microscope using a 1.4 NA PlanApo 100× oil objective lens (Nikon). Lasers used for excitation were 561 nm 50 mW (MPB Lasertech) and 405 nm 50 mW CUBE (Coherent). Power levels, measured at the back aperture of the objective lens, ranged 11 mW (estimated 1 kW/cm^2 at a sample) for the 561 nm laser, and 1 to 10 μW (estimated 0.1 to 1 W/cm^2 at a sample) for the 405 nm laser. We used a quadruple-band dichroic mirror (Di01-R405/488/561/640, Semrock), and emission light is further filtered using a band-pass filter centered at 617 nm (FF01-617/70, Semrock).

Fluorescence was detected with a back-illuminated electron-multiplying charge-coupled device (EMCCD) camera (Andor Technology, Ixon3 DU897E, 10 MHz EM amplifier, 250× gain, 128 × 128 optically centered "Cropped Mode" region of interest) at a frame rate of 33.3 frames per second. Five thousand consecutive frames of photoswitched PSLSSmKate-β-actin and PATagRFP-β-actin were used in the comparison analysis. The cells were continuously and simultaneously illuminated with a low-power 405 nm laser (0.1 W/cm^2) so that a fraction of PSLSSmKate or PATagRFP molecules photoconverted in each frame. The same setup was used to image H2B-PSLSSmKate in live U2OS cells (Figure 4B), where 10,000 consecutive frames were recorded at a frame rate of 20 frames/s using a low-power continuous 405 nm laser for continuous photoconversion of PSLSSmKate. Ten thousand consecutive frames of PSLSSmKate-β-actin were also recorded on a custom-built microscope with stroboscopic 405 nm excitation (Figure 4A). The stroboscopic illumination was achieved using a NI-DAQ-USB-6363 acquisition board (National Instruments) as a pulse generator as previously described (English et al., 2011). PALM data in Figure 4A were recorded on a custom-built three-camera RAMM frame microscope (ASI) using an Olympus 1.4 NA PLAPON 60 × OSC objective, and a custom tube lens (LAO-300.0, Melles Griot), resulting in 100× overall magnification. A 2 mm thick quad-band excitation dichroic (ZT405/488/561/640rpc, Chroma), a 2 mm thick emission dichroic (T560lpxr, Chroma), and a band-pass emission filter (FF01-609/54-25, Semrock) filtered the emitted light. Fluorescence was detected with a back-illuminated EMCCD camera (Andor Technology, Ixon Ultra DU-897U, 17 MHz EM amplifier, 200× gain, full-chip) at 20 frames/s. PSLSSmKate was photoconverted by 5 ms long excitation pulses of 405 nm (10 W/cm^2) every 500 ms. The frames containing conversion pulses were manually removed before further analysis.

Individual molecules were localized using Diatrack (version 3.03, Semasopht), which identifies and fits the intensity spots of our fluorescent particles with symmetric 2D Gaussian functions with a width matched to the experimentally determined point-spread function. For each detected particle, integrated fluorescence intensities were calculated and converted to photon counts using analysis routines written in IGOR Pro version 6.32A. Localized molecules were rendered corresponding to their localization errors using the software ViSP (El Beheiry and Dahan, 2013). The mean localization errors were determined using Equation 6 in reference (Mortensen et al., 2010).

MS Analysis

Aliquots of 25 μg of the intact and illuminated 6xHistagged PSLSSmKate protein were denatured by heating in 15 μl of 4.8 M guanidine chloride at 80°C for 3 min. Then the samples were cooled to room temperature. Thirty microliters of 50 mM NH_4HCO_3 (pH 7.8) and 15 μl of water were added, and then trypsin was added at an enzyme/protein ratio of 1:60. The digests were incubated at room temperature (24°C) for 22 hr and quenched with 0.1% trifluoroacetic acid (TFA).

Peptides were separated using a Dionex UltiMate 3000 Nano LC system (Dionex) that consisted of an Acclaim PepMap 100 C18 nanoLC analytical column (3 μm, 0.075 × 150 mm) and an Acclaim PepMap μ-precolumn for desalting (0.03 × 5 mm). The mobile phases (MPs) used were as follows: MP-A was 950:50:1 high-performance liquid chromatography (HPLC)-grade water/HPLC-grade acetonitrile/TFA (v/v/v), and MP-B was 950:50:1 HPLC-grade acetonitrile/HPLC-grade water/TFA (v/v/v). The chromatographic gradient profile for peptide separation was (min/MP-B%) 0.0/2.0, 20.0/2.0, 60.0/42.0, 65.0/90.0, 75.0/90.0, 80.0/2.0, and 95.0/2.0. The MP flow rate was 0.25 μl/min, and the eluted peptides were mixed with the α-CHC matrix solution and fractionated onto a MALDI plate (32.5 nL of the eluted peptides/spot) automatically using the Probot MALDI spotter (Dionex).

Collected peptide fractions were analyzed offline using a MALDI/TOF mass spectrometer (ABI 4800 Proteomics TOF/TOF Analyzer, Applied Biosystems) in positive reflector mode. The MS settings were as following: mass range 800 to 4,000 Da, focus mass 1,500 Da, fixed laser intensity 3,500, bin size 0.5 ns, vertical scale 0.5 V, vertical offset 0.2% of full scale, input bandwidth 500 MHz, detector voltage multiplier 0.82, and final detector voltage 1.796. MS/MS were acquired in a PSD mode with mass isolation window of ±3 Da.

Crystallization, X-Ray Diffraction Data Collection, and Crystallographic Refinement

Diffraction quality crystals were grown by sitting drop vapor diffusion by mixing 1 μl of protein (PSLSSmKate concentration was 11 mg/mL in 10 mM NaH_2PO_4 [pH 7.5]) with 1 μl of reservoir solution and equilibrating the samples against the corresponding reservoir solution. The reservoir solution contained 25% polyethylene glycol 3350, 0.1 M citric acid (pH 3.5). Crystals of PSLSSmKate with dimensions 0.2 × 0.2 × 0.2 mm^3 were mounted in cryoloops directly from the crystallization droplet and flash-cooled in liquid nitrogen. Before freezing, a final concentration of 20% glycerol was added (as a cryoprotectant) to the droplets. Diffraction data were recorded on a Quantum 315 CCD detector (Area Detector Systems) with 0.979 Å wavelength radiation on the Northeastern Collaborative Access Team (NE-CAT) beamline (Advanced Photon Source). Intensities were integrated using the HKL2000 program and reduced to amplitudes using the SCALEPACK2MTZ program (see Table S1 for statistics) (French and Wilson, 1978; Otwinowski and Minor, 1997; Winn et al., 2011). Structures were determined by molecular replacement with PHASER (McCoy et al., 2007). Model building and refinement were performed with the programs COOT and REFMAC, respectively (Emsley et al., 2010; Murshudov et al., 1997). The quality of the final structures was verified with composite omit maps, and stereochemistry was checked with the program MOLPROBITY (Davis et al., 2007). LSQKAB and SSM algorithms were used for structural superpositions (Kabsch, 1976; Krissinel and Henrick, 2004). All other calculations were performed with the CCP4 program suite (Winn et al., 2011).

ACCESSION NUMBERS

The coordinates of PSLSSmKate crystal were submitted to the Protein Data Bank (PDB) with the accession number 4NWS.

SUPPLEMENTAL INFORMATION

Supplemental Information includes ten figures and one table and can be found with this article online at http://dx.doi.org/10.1016/j.chembiol.2014.08.010.

ACKNOWLEDGMENTS

We thank Jeffrey Segall and Jacco van Rheenen for plasmids, Rafael Toro for assistance with protein crystallization, Udupi Ramagopal and the NE-CAT beamline staff at the Advanced Photon Source for help with X-ray data collection, and Konstantin Rumyantsev for help with characterization of PSLSSmKate mutants. This work was supported by grants GM073913, GM108579, EB013571, GM094662 (New York Structural Genomics Research Center), and CA013330 (Albert Einstein Cancer Center) from the NIH and ERC-2013-ADG-340233 from the European Union's FP7 program.

Received: March 3, 2014
Revised: August 8, 2014
Accepted: August 13, 2014
Published: September 18, 2014

REFERENCES

Ai, H.W., Hazelwood, K.L., Davidson, M.W., and Campbell, R.E. (2008a). Fluorescent protein FRET pairs for ratiometric imaging of dual biosensors. Nat. Methods *5*, 401–403.

Ai, H.W., Olenych, S.G., Wong, P., Davidson, M.W., and Campbell, R.E. (2008b). Hue-shifted monomeric variants of Clavularia cyan fluorescent protein: identification of the molecular determinants of color and applications in fluorescence imaging. BMC Biol. *6*, 13.

Bell, A.F., Stoner-Ma, D., Wachter, R.M., and Tonge, P.J. (2003). Light-driven decarboxylation of wild-type green fluorescent protein. J. Am. Chem. Soc. *125*, 6919–6926.

Brejc, K., Sixma, T.K., Kitts, P.A., Kain, S.R., Tsien, R.Y., Ormö, M., and Remington, S.J. (1997). Structural basis for dual excitation and photoisomerization of the Aequorea victoria green fluorescent protein. Proc. Natl. Acad. Sci. USA *94*, 2306–2311.

Bublitz, G., King, B.A., and Boxer, S.G. (1998). Electronic structure of the chromophore in green fluorescent protein (GFP). J. Am. Chem. Soc. *120*, 9370–9371.

Chalfie, M., Tu, Y., Euskirchen, G., Ward, W.W., and Prasher, D.C. (1994). Green fluorescent protein as a marker for gene expression. Science *263*, 802–805.

Chattoraj, M., King, B.A., Bublitz, G.U., and Boxer, S.G. (1996). Ultra-fast excited state dynamics in green fluorescent protein: multiple states and proton transfer. Proc. Natl. Acad. Sci. USA *93*, 8362–8367.

Chica, R.A., Moore, M.M., Allen, B.D., and Mayo, S.L. (2010). Generation of longer emission wavelength red fluorescent proteins using computationally designed libraries. Proc. Natl. Acad. Sci. USA *107*, 20257–20262.

Chu, J., Haynes, R.D., Corbel, S.Y., Li, P., González-González, E., Burg, J.S., Ataie, N.J., Lam, A.J., Cranfill, P.J., Baird, M.A., et al. (2014). Non-invasive intravital imaging of cellular differentiation with a bright red-excitable fluorescent protein. Nat. Methods *11*, 572–578.

Chudakov, D.M., Matz, M.V., Lukyanov, S., and Lukyanov, K.A. (2010). Fluorescent proteins and their applications in imaging living cells and tissues. Physiol. Rev. *90*, 1103–1163.

Cubitt, A.B., Heim, R., Adams, S.R., Boyd, A.E., Gross, L.A., and Tsien, R.Y. (1995). Understanding, improving and using green fluorescent proteins. Trends Biochem. Sci. *20*, 448–455.

Davis, I.W., Leaver-Fay, A., Chen, V.B., Block, J.N., Kapral, G.J., Wang, X., Murray, L.W., Arendall, W.B., 3rd, Snoeyink, J., Richardson, J.S., and Richardson, D.C. (2007). MolProbity: all-atom contacts and structure validation for proteins and nucleic acids. Nucleic Acids Res. *35*, W375–W383.

El Beheiry, M., and Dahan, M. (2013). ViSP: representing single-particle localizations in three dimensions. Nat. Methods *10*, 689–690.

Emsley, P., Lohkamp, B., Scott, W.G., and Cowtan, K. (2010). Features and development of Coot. Acta Crystallogr. D Biol. Crystallogr. *66*, 486–501.

English, B.P., Hauryliuk, V., Sanamrad, A., Tankov, S., Dekker, N.H., and Elf, J. (2011). Single-molecule investigations of the stringent response machinery in living bacterial cells. Proc. Natl. Acad. Sci. USA *108*, E365–E373.

French, S., and Wilson, K. (1978). On the treatment of negative intensity observations. Acta Crystallogr. A *34*, 517–525.

Habuchi, S., Cotlet, M., Gensch, T., Bednarz, T., Haber-Pohlmeier, S., Rozenski, J., Dirix, G., Michiels, J., Vanderleyden, J., Heberle, J., et al. (2005). Evidence for the isomerization and decarboxylation in the photoconversion of the red fluorescent protein DsRed. J. Am. Chem. Soc. *127*, 8977–8984.

Henderson, J.N., Gepshtein, R., Heenan, J.R., Kallio, K., Huppert, D., and Remington, S.J. (2009a). Structure and mechanism of the photoactivatable green fluorescent protein. J. Am. Chem. Soc. *131*, 4176–4177.

Henderson, J.N., Osborn, M.F., Koon, N., Gepshtein, R., Huppert, D., and Remington, S.J. (2009b). Excited state proton transfer in the red fluorescent protein mKeima. J. Am. Chem. Soc. *131*, 13212–13213.

Isom, D.G., Castañeda, C.A., Cannon, B.R., Velu, P.D., and García-Moreno E, B. (2010). Charges in the hydrophobic interior of proteins. Proc. Natl. Acad. Sci. USA *107*, 16096–16100.

Jeffrey, G.A. (1997). An Introduction to Hydrogen Bonding. (New York: Oxford University Press).

Kabsch, W. (1976). A solution for the best rotation to relate two sets of vectors. Acta Crystallogr. A *32*, 922–923.

Krissinel, E., and Henrick, K. (2004). Secondary-structure matching (SSM), a new tool for fast protein structure alignment in three dimensions. Acta Crystallogr. D Biol. Crystallogr. *60*, 2256–2268.

Matsuda, T., Miyawaki, A., and Nagai, T. (2008). Direct measurement of protein dynamics inside cells using a rationally designed photoconvertible protein. Nat. Methods *5*, 339–345.

McCoy, A.J., Grosse-Kunstleve, R.W., Adams, P.D., Winn, M.D., Storoni, L.C., and Read, R.J. (2007). Phaser crystallographic software. J. Appl. Cryst. *40*, 658–674.

Miyawaki, A., Shcherbakova, D.M., and Verkhusha, V.V. (2012). Red fluorescent proteins: chromophore formation and cellular applications. Curr. Opin. Struct. Biol. *22*, 679–688.

Mortensen, K.I., Churchman, L.S., Spudich, J.A., and Flyvbjerg, H. (2010). Optimized localization analysis for single-molecule tracking and super-resolution microscopy. Nat. Methods *7*, 377–381.

Murshudov, G.N., Vagin, A.A., and Dodson, E.J. (1997). Refinement of macromolecular structures by the maximum-likelihood method. Acta Crystallogr. D Biol. Crystallogr. *53*, 240–255.

Otwinowski, Z., and Minor, W. (1997). Processing of X-ray diffraction data collected in oscillation mode. Methods Enzymol. *276*, 307–326.

Palm, G.J., Zdanov, A., Gaitanaris, G.A., Stauber, R., Pavlakis, G.N., and Wlodawer, A. (1997). The structural basis for spectral variations in green fluorescent protein. Nat. Struct. Biol. *4*, 361–365.

Piatkevich, K.D., and Verkhusha, V.V. (2010). Advances in engineering of fluorescent proteins and photoactivatable proteins with red emission. Curr. Opin. Chem. Biol. *14*, 23–29.

Piatkevich, K.D., Hulit, J., Subach, O.M., Wu, B., Abdulla, A., Segall, J.E., and Verkhusha, V.V. (2010a). Monomeric red fluorescent proteins with a large Stokes shift. Proc. Natl. Acad. Sci. USA *107*, 5369–5374.

Piatkevich, K.D., Malashkevich, V.N., Almo, S.C., and Verkhusha, V.V. (2010b). Engineering ESPT pathways based on structural analysis of LSSmKate red fluorescent proteins with large Stokes shift. J. Am. Chem. Soc. *132*, 10762–10770.

Piatkevich, K.D., Malashkevich, V.N., Morozova, K.S., Nemkovich, N.A., Almo, S.C., and Verkhusha, V.V. (2013). Extended Stokes shift in fluorescent proteins: chromophore-protein interactions in a near-infrared TagRFP675 variant. Sci. Rep. *3*, 1847.

Randino, C., Moreno, M., Gelabert, R., and Lluch, J.M. (2012). Peek at the potential energy surfaces of the LSSmKate1 and LSSmKate2 proteins. J. Phys. Chem. B *116*, 14302–14310.

Shcherbakova, D.M., Hink, M.A., Joosen, L., Gadella, T.W., and Verkhusha, V.V. (2012a). An orange fluorescent protein with a large Stokes shift for single-excitation multicolor FCCS and FRET imaging. J. Am. Chem. Soc. *134*, 7913–7923.

Shcherbakova, D.M., Subach, O.M., and Verkhusha, V.V. (2012b). Red fluorescent proteins: advanced imaging applications and future design. Angew. Chem. Int. Ed. Engl. *51*, 10724–10738.

Shcherbo, D., Murphy, C.S., Ermakova, G.V., Solovieva, E.A., Chepurnykh, T.V., Shcheglov, A.S., Verkhusha, V.V., Pletnev, V.Z., Hazelwood, K.L., Roche, P.M., et al. (2009). Far-red fluorescent tags for protein imaging in living tissues. Biochem. J. *418*, 567–574.

Shu, X., Shaner, N.C., Yarbrough, C.A., Tsien, R.Y., and Remington, S.J. (2006). Novel chromophores and buried charges control color in mFruits. Biochemistry *45*, 9639–9647.

Subach, F.V., and Verkhusha, V.V. (2012). Chromophore transformations in red fluorescent proteins. Chem. Rev. *112*, 4308–4327.

Subach, F.V., Malashkevich, V.N., Zencheck, W.D., Xiao, H., Filonov, G.S., Almo, S.C., and Verkhusha, V.V. (2009). Photoactivation mechanism of PAmCherry based on crystal structures of the protein in the dark and fluorescent states. Proc. Natl. Acad. Sci. USA *106*, 21097–21102.

Subach, F.V., Patterson, G.H., Renz, M., Lippincott-Schwartz, J., and Verkhusha, V.V. (2010a). Bright monomeric photoactivatable red fluorescent protein for two-color super-resolution sptPALM of live cells. J. Am. Chem. Soc. *132*, 6481–6491.

Subach, O.M., Malashkevich, V.N., Zencheck, W.D., Morozova, K.S., Piatkevich, K.D., Almo, S.C., and Verkhusha, V.V. (2010b). Structural characterization of acylimine-containing blue and red chromophores in mTagBFP and TagRFP fluorescent proteins. Chem. Biol. *17*, 333–341.

Subach, F.V., Piatkevich, K.D., and Verkhusha, V.V. (2011a). Directed molecular evolution to design advanced red fluorescent proteins. Nat. Methods *8*, 1019–1026.

Subach, O.M., Patterson, G.H., Ting, L.-M., Wang, Y., Condeelis, J.S., and Verkhusha, V.V. (2011b). A photoswitchable orange-to-far-red fluorescent protein, PSmOrange. Nat. Methods *8*, 771–777.

Subach, O.M., Entenberg, D., Condeelis, J.S., and Verkhusha, V.V. (2012). A FRET-facilitated photoswitching using an orange fluorescent protein with the fast photoconversion kinetics. J. Am. Chem. Soc. *134*, 14789–14799.

Thompson, M.A., Biteen, J.S., Lord, S.J., Conley, N.R., and Moerner, W.E. (2010). Molecules and methods for super-resolution imaging. Methods Enzymol. *475*, 27–59.

van Thor, J.J., Gensch, T., Hellingwerf, K.J., and Johnson, L.N. (2002). Phototransformation of green fluorescent protein with UV and visible light leads to decarboxylation of glutamate 222. Nat. Struct. Biol. *9*, 37–41.

Violot, S., Carpentier, P., Blanchoin, L., and Bourgeois, D. (2009). Reverse pH-dependence of chromophore protonation explains the large Stokes shift of the red fluorescent protein mKeima. J. Am. Chem. Soc. *131*, 10356–10357.

Winn, M.D., Ballard, C.C., Cowtan, K.D., Dodson, E.J., Emsley, P., Evans, P.R., Keegan, R.M., Krissinel, E.B., Leslie, A.G.W., McCoy, A., et al. (2011). Overview of the CCP4 suite and current developments. Acta Crystallogr. D Biol. Crystallogr. *67*, 235–242.

Wu, B., Piatkevich, K.D., Lionnet, T., Singer, R.H., and Verkhusha, V.V. (2011). Modern fluorescent proteins and imaging technologies to study gene expression, nuclear localization, and dynamics. Curr. Opin. Cell Biol. *23*, 310–317.

Zapata-Hommer, O., and Griesbeck, O. (2003). Efficiently folding and circularly permuted variants of the Sapphire mutant of GFP. BMC Biotechnol. *3*, 5.

Zhang, M.Y., Wang, J.Y., Lin, C.S., and Cheng, W.D. (2011). First-principles study of one- and two-photon absorption of the H-bonding complexes from monomeric red fluorescent proteins with large Stokes shifts. J. Phys. Chem. B *115*, 10750–10757.

Chemistry & Biology, Volume *21*

Supplemental Information

Photoswitchable Red Fluorescent Protein with a Large Stokes Shift

Kiryl D. Piatkevich, Brian P. English, Vladimir N. Malashkevich, Hui Xiao, Steven C. Almo, Robert H. Singer, and Vladislav V. Verkhusha

Figure S1, related to Figure 1.

Alignment of the amino acid sequences of PSLSSmKate and LSSmKate1.

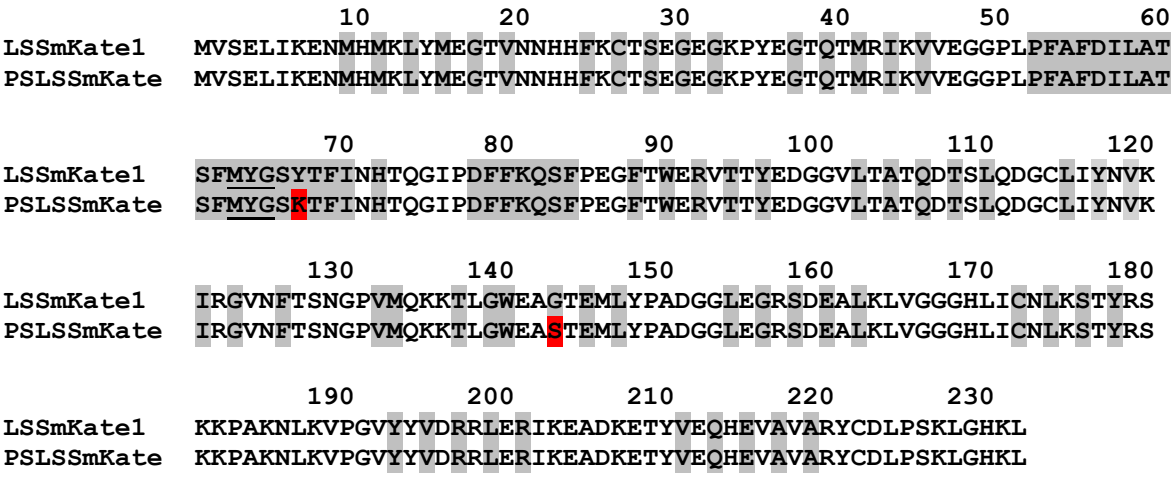

The internal amino acid residues are highlighted in gray. The chromophore-forming amino acid residues are underlined. Mutations resulting in the conversion of parental LSSmKate1 into PSLSSmKate are shown in red.

Figure S2, related to Figure 1.

Semi-native polyacrylamide gel with purified fluorescent proteins including PSLSSmKate.

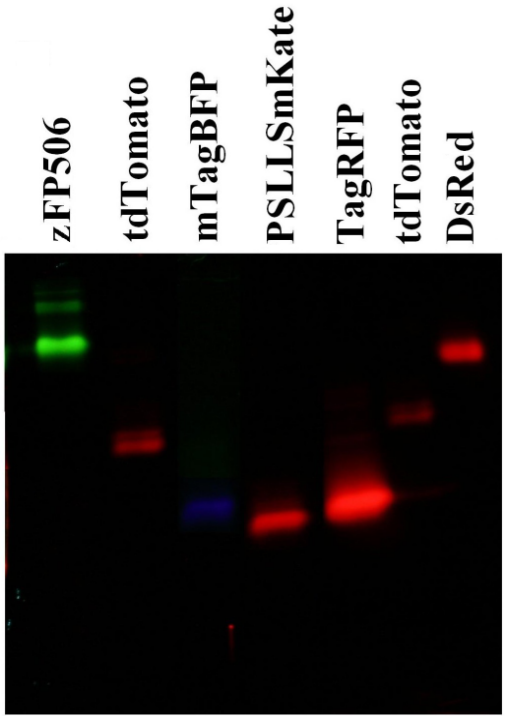

Freshly purified samples with concentration of corresponding fluorescent protein 1 mg/ml were applied in 10 µl aliquots to semi-native 15% polyacrylamide gels containing 0.1% SDS. The protein amounts were 10 µg per lane. The gels were photographed using a Leica MZ16FL fluorescence stereomicroscope. zFP506 and DsRed were used as the tetrameric native protein standards, tdTomato as dimeric, mTagBFP and TagRFP as monomeric. 436⁄20 nm excitation and 595 nm LP emission filters were applied to image PSLSSmKate; and 570⁄30 nm excitation and 595 nm LP emission filters were applied to image tdTomato and DsRed; and 480⁄40 nm excitation and 530/40 nm emission filters were applied to image zFP506; and 390⁄40 nm excitation and 460/40 nm emission filters were applied to image mTagBFP.

Figure S3, related to Figure 1.

Wide-field fluorescence microscopy of the PSLSSmKate fusion proteins expressed in various live mammalian cells.

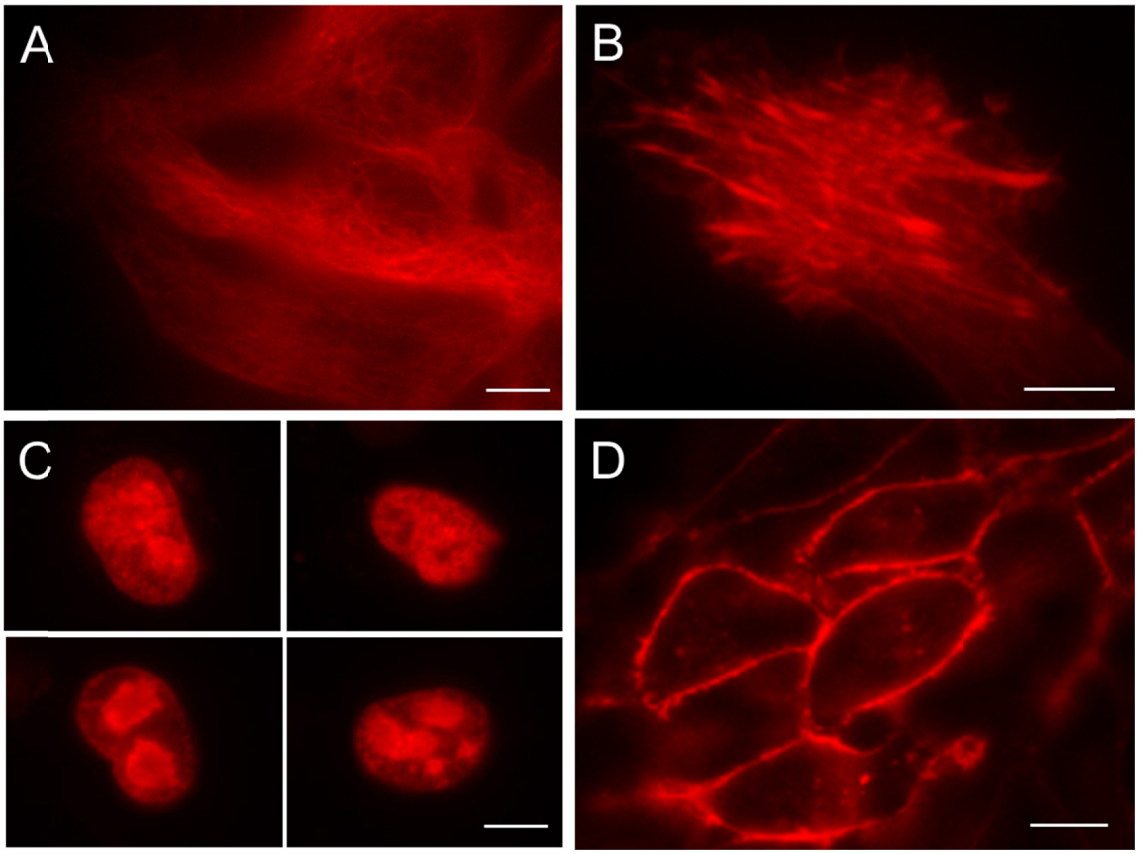

HeLa cells transfected with (A) PSLSSmKate-α-tubulin and (B) PSLSSmKate-β-actin, (C) Cos-7 cells transfected with histone H3.2-PSLSSmKate, and (D) MTLn3 cells transfected with PSLSSmKate-CAAX are shown. Scale bars are 10 μm.

Figure S4, related to Figure 1.

Wide-field fluorescent images of live HeLa cells transiently transfected with untagged PSLSSmKate.

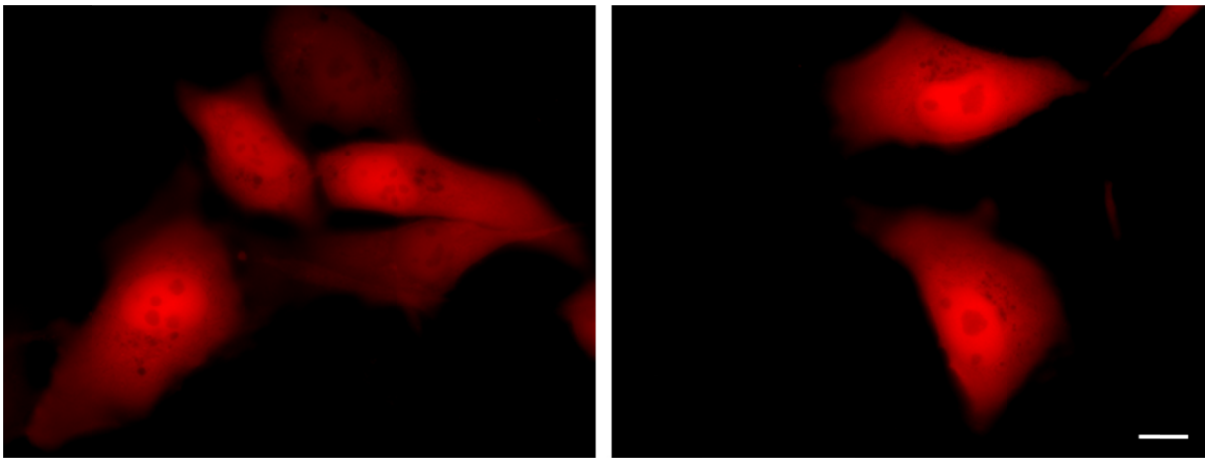

The fluorescence of PSLSSmKate was evenly distributed within the cytosol and nucleus of the live cells without any aggregation or nonspecific localization. Scale bar is 10 μm.

Figure S5, related to Figure 1.

Changes of the fluorescence signals of photoswitched PSLSSmKate.

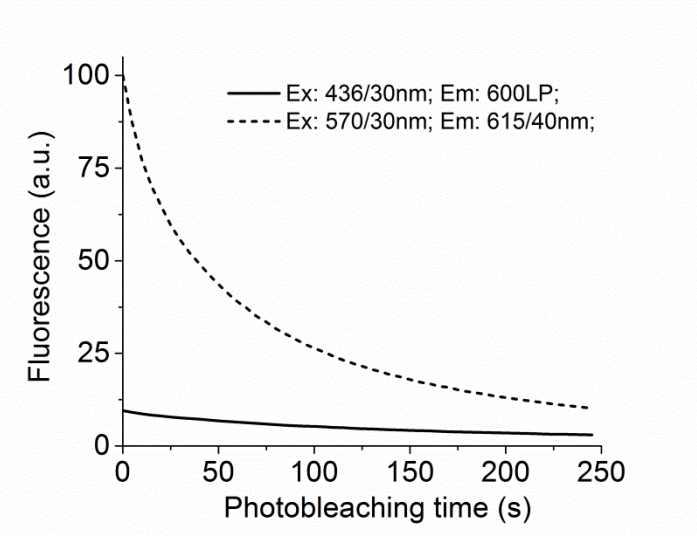

The changes recorded using Ex: 436/20 nm and Em: 600 nm LP, and Ex: 570/30 nm and Em: 615/40 nm filter sets under continuous 570/30 nm illumination. The photobleaching experiments performed in live HeLa cells expressing untagged PSLSSmKate using wide-field microscope with 60x oil immersion objective. Before photobleaching of the red form PSLSSmKate was completely photoswitched using 390/40 nm light.

Figure S6, related to Figure 5.

Molecular structure of the PSLSSmKate chromophore superimposed onto the refined 2Fo-Fc electron density.

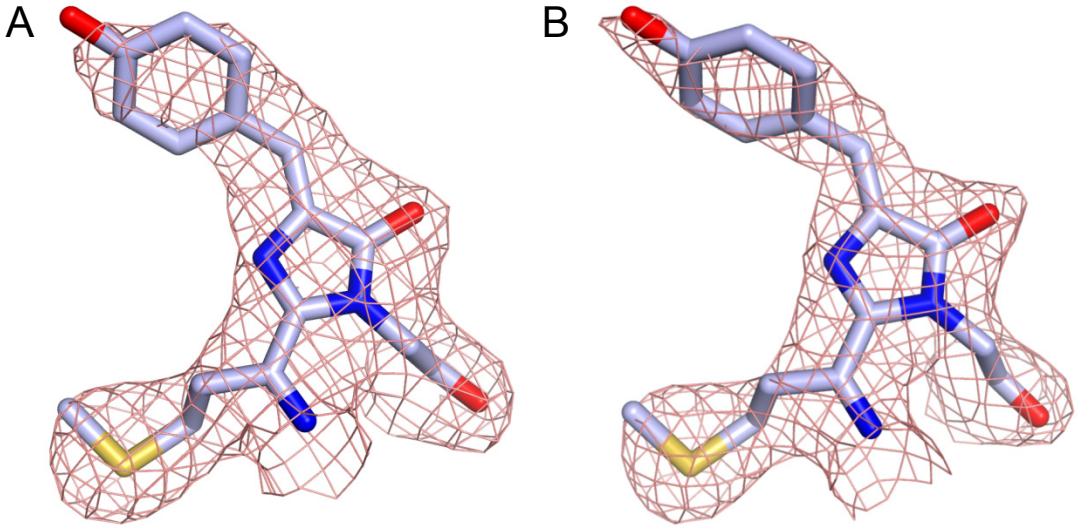

(A) A subunit and (B) B subunit. The chromophore predominantly adopts the *cis*-configuration in both subunits.

Figure S7, related to Figure 5.

MS/MS spectra of the I202-R220 peptide of PSLSSmKate.

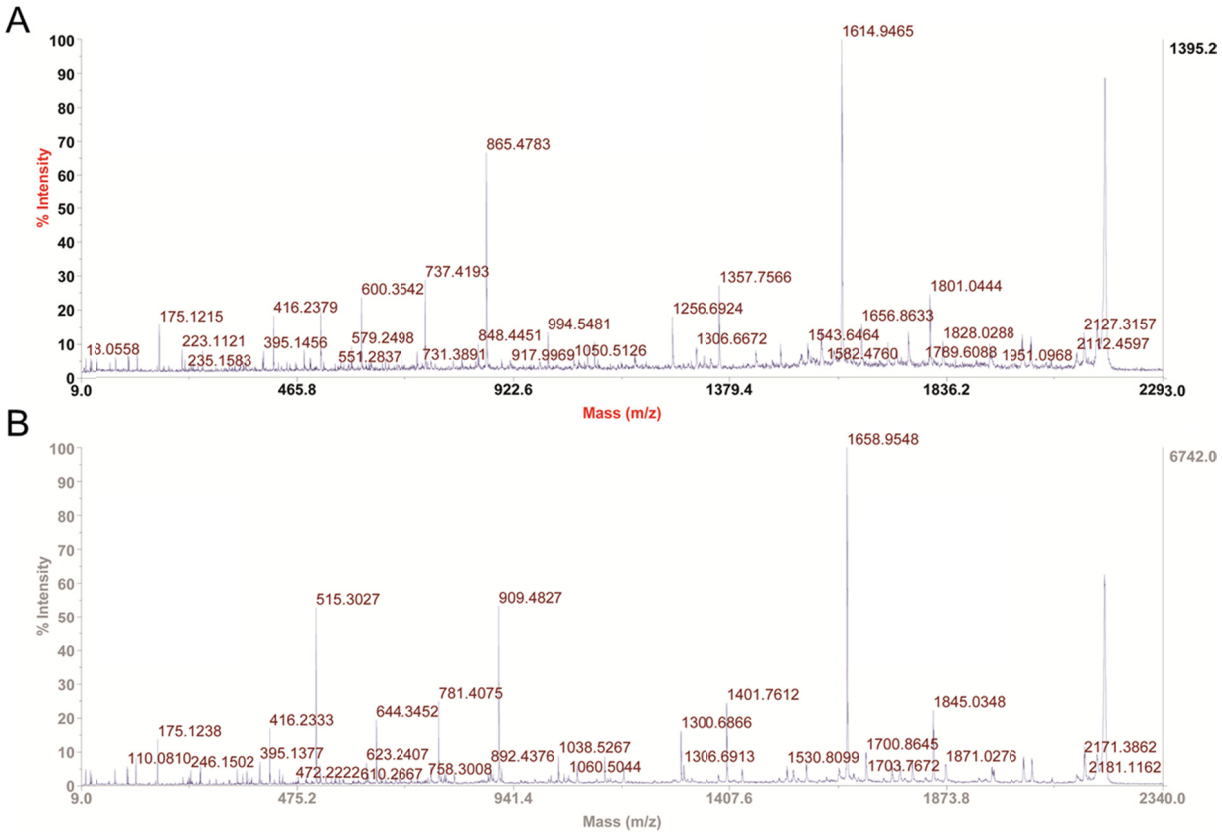

The MS/MS spectra of the I202-R220 peptide isolated from the trypsinized samples of the purified PSLSSmKate are shown (A) before and (B) after illumination with 405 nm LED array.

Figure S8, related to Table 2.

Fluorescence excitation and emission spectra for PSLSSmKate and its single-point mutants.

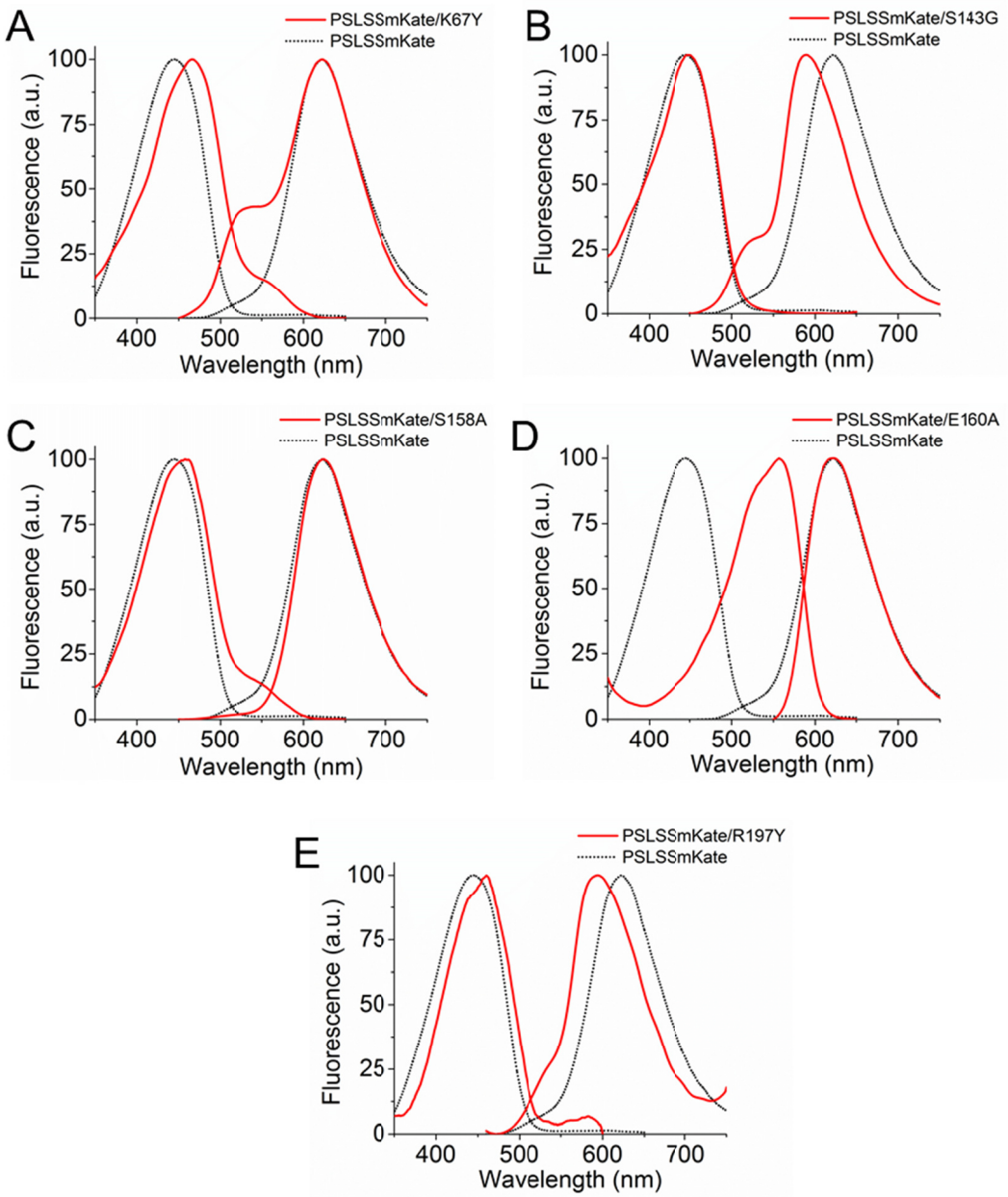

Fluorescence excitation and emission spectra are shown for (A) PSLSSmKate/K67Y (solid red line) and LSSmKate1 (dotted black line), (B) PSLSSmKate/S143G (solid red line) and LSSmKate1 (dotted black line), (C) PSLSSmKate/S158A (solid red line) and LSSmKate1 (dotted black line), (D) PSLSSmKate/E160A (solid red line) and LSSmKate1 (dotted black line), and (E) PSLSSmKate/R197Y (solid red line) and LSSmKate1 (dotted black line).

Figure S9, related to Table 2.

Changes in red fluorescence of PSLSSmKate, its single-point mutants and LSSmKate1.

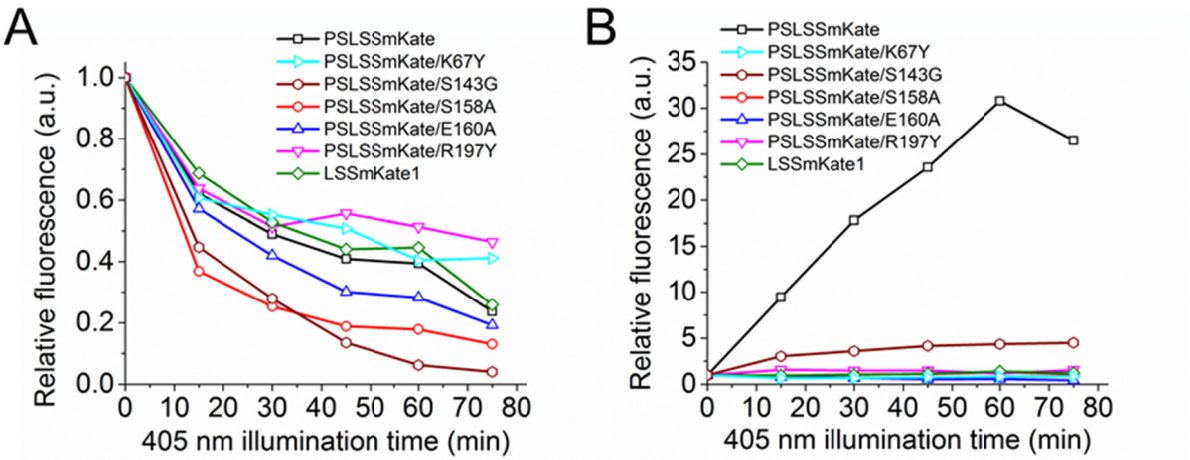

Changes in red fluorescence of PSLSSmKate, its point mutants and parental LSSmKate1 were measured using excitation (A) at 445 nm and (B) at 560 nm under continuous illumination of 405 nm LED array at light power 90 mW/cm^2.

Figure S10, related to Table 1.

Fluorescence excitation and emission spectra for PSLSSmKate and LSSmKate1.

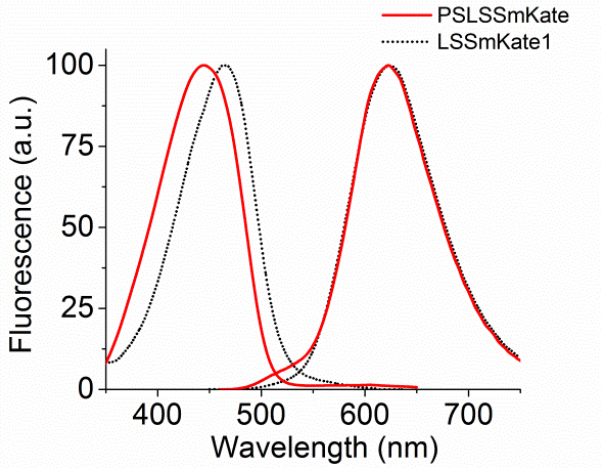

Fluorescence excitation and emission spectra are shown for PSLSSmKate (solid red line) and parental LSSmKate1 (dotted black line).

Table S1, related to Figure 5.
Data collection and refinement statistics of the PSLSSmKate

Data Collection	
Wavelength (Å)	0.979
Space group	I4
Unit cell dimensions (Å)	a= b= 99.03 c= 106.61 α=β=γ=90°,
Resolution range (Å)	38.0- 2.7
Observed reflections	67,759
Unique reflections	12,943
Completeness (%) [a]	91.5 (34.8)
I/σI	10.2 (3.0)
R-merge (I) [b]	0.078(0.336)
Structure Refinement	
R_{cryst} (%) [c]	0.182 (0.242)
R_{free} (%) [c]	0.253 (0.302)
Total nonhydrogen atoms	3,674
Protein	3,531
Water molecules	97
Heterogen atoms	46
Average B-factor (Å^2)	44.9
Protein	45.3
Water molecules	37.7
RMS Deviations from ideal value	
Bonds (Å)	0.008
Angles (°)	1.43
Torsion angles (°)	17.8
Overall coordinate error	
Based on R-factor	0.083
Ramachandran plot	
Most favored (%)	99.5

[a] Values in parentheses indicate statistics for the highest resolution shell: 2.77-2.70.
[b] $R_{merge} = \Sigma\Sigma\, j|Ij(hkl) - \langle I(hkl)\rangle| / \Sigma\Sigma\, j|\langle I(hkl)\rangle|$, where Ij is the intensity measurement for reflection j and <I> is the mean intensity over j reflections.
[c] $R_{cryst}/(R_{free}) = \Sigma\, ||F_o(hkl)| - |F_c(hkl)|| / \Sigma\, |F_o(hkl)|$, where F_o and F_c are observed and calculated structure factors, respectively. No σ-cutoff was applied. 5% of the reflections were excluded from refinement and used to calculate R_{free}.